J. Fluid Mech. (2018), *vol.* 855, *pp.* 371–407. © Cambridge University Press 2018
doi:10.1017/jfm.2018.644

Large-eddy simulation of flow over a rotating cylinder: the lift crisis at $Re_D = 6 \times 10^4$

W. Cheng[1,2,†], D. I. Pullin[2] and R. Samtaney[1]

[1]Mechanical Engineering, Physical Science and Engineering Division, King Abdullah University of Science and Technology, Thuwal, Saudi Arabia, 23955-6900

[2]Graduate Aerospace Laboratories, California Institute of Technology, CA 91125, USA

(Received 22 February 2018; revised 28 June 2018; accepted 5 August 2018;
first published online 19 September 2018)

We present wall-resolved large-eddy simulation (LES) of flow with free-stream velocity $\boldsymbol{U}_\infty$ over a cylinder of diameter D rotating at constant angular velocity Ω, with the focus on the lift crisis, which takes place at relatively high Reynolds number $Re_D = U_\infty D/\nu$, where ν is the kinematic viscosity of the fluid. Two sets of LES are performed within the (Re_D, α)-plane with $\alpha = \Omega D/(2U_\infty)$ the dimensionless cylinder rotation speed. One set, at $Re_D = 5000$, is used as a reference flow and does not exhibit a lift crisis. Our main LES varies α in $0 \leqslant \alpha \leqslant 2.0$ at fixed $Re_D = 6 \times 10^4$. For α in the range $\alpha = 0.48$–0.6 we find a lift crisis. This range is in agreement with experiment although the LES shows a deeper local minimum in the lift coefficient than the measured value. Diagnostics that include instantaneous surface portraits of the surface skin-friction vector field $\boldsymbol{C}_f$, spanwise-averaged flow-streamline plots, and a statistical analysis of local, near-surface flow reversal show that, on the leeward-bottom cylinder surface, the flow experiences large-scale reorganization as α increases through the lift crisis. At $\alpha = 0.48$ the primary-flow features comprise a shear layer separating from that side of the cylinder that moves with the free stream and a pattern of oscillatory but largely attached flow zones surrounded by scattered patches of local flow separation/reattachment on the lee and underside of the cylinder surface. Large-scale, unsteady vortex shedding is observed. At $\alpha = 0.6$ the flow has transitioned to a more ordered state where the small-scale separation/reattachment cells concentrate into a relatively narrow zone with largely attached flow elsewhere. This induces a low-pressure region which produces a sudden decrease in lift and hence the lift crisis. Through this process, the boundary layer does not show classical turbulence behaviour. As α is further increased at constant Re_D, the localized separation zone dissipates with corresponding attached flow on most of the cylinder surface. The lift coefficient then resumes its increasing trend. A logarithmic region is found within the boundary layer at $\alpha = 1.0$.

Key words: boundary layer separation, boundary layers, turbulence simulation

1. Introduction

The drag crisis for flow over a smooth, non-rotating cylinder, where a sharp decrease of the drag coefficient occurs over a relatively narrow band of Reynolds

† Email address for correspondence: chengw@caltech.edu

number Re_D, was first noted by Taylor around 1915 (Dryden, Murnaghan & Bateman 1932). A widely accepted interpretation of the drag crisis is centred on the onset of flow transition to turbulence that occurs initially on the separating shear layer on one side of the cylinder and which then migrates to the upstream boundary layer. This produces a robust near-wall flow that better resists the adverse pressure gradient, leading to a subsequent downstream movement of the primary-separation zone, and reduces pressure drag. A related phenomenon is the presence of a mean-flow, secondary-separation bubble which resides within the primary-separation zone for subcritical flow (Son & Hanratty 1969), moving upstream of the primary-separation bubble as Re_D reaches the supercritical regime (Schewe 1983).

Large-eddy simulation (LES) by Lehmkuhl *et al.* (2014) showed a mean-flow separation bubble upstream of the primary-separation zone at supercritical Re_D. Cheng *et al.* (2017) investigated the detailed near-surface flow behaviour through the drag crisis using LES. Their azimuthal skin-friction profiles at $Re_D = 8.5 \times 10^5$ capture boundary-layer transition and agree well with experiments by Achenbach (1968). Cheng *et al.* (2017) observed local mean-flow separation bubbles at both subcritical and supercritical Re_D. They hypothesize that the drag crisis is a consequence of a global change in the overall flow state produced by the interaction of unsteady, secondary flow reattachment cells, visible as bundles of diverging surface streamlines within the large-scale separation region, with the principal separation shear layer. They further argue that boundary-layer laminar–turbulent transition is not itself the dynamical agent of the drag crisis but instead is an effect of this changed flow state. Some evidence supporting this interpretation is provided by Cheng, Pullin & Samtaney (2018), who find a drag crisis for flow past a grooved cylinder where well-developed boundary layers do not exist.

When the cylinder rotates about its axis with constant angular velocity Ω, a new parameter, the non-dimensional rotation speed $\alpha = \Omega D/(2U_\infty)$ is introduced, resulting in cylinder top–bottom flow asymmetry. Initial experimental studies (Reid 1924; Thom 1931) showed that the lift coefficient C_L generally increases as α increases at fixed Re_D. A significant portion of the Re_D–α plane was explored experimentally by Swanson (1961), who found that, at fixed Re_D greater than approximately $Re_D = 3.58 \times 10^4$, C_L decreased almost discontinuously and then continued to increase as α passed through a small range that depended on Re_D. This so-called lift crisis has been confirmed in subsequent experiments (Fletcher 1972; Takayama & Aoki 2005). The fluid-dynamical mechanisms active during the lift crisis are not well understood. Swanson (1961) suggests that the boundary layer on the bottom, or counter-flow side of the cylinder (where the cylinder surface velocity opposes the free-stream velocity), transitions to turbulence when C_L begins to decrease, and reaches a fully developed turbulent state when C_L is near its local minimum value. This then affects the azimuthal location of separation with subsequent changes in C_L. While later studies, for example, Fletcher (1972), adopt this explanation, there appears to be a dearth of supporting experimental or numerical evidence. We note that the lift crisis, also referred to as the inverse Magnus effect, is also observed in other flows over rotating bluff bodies – for example, flow over a rotating sphere (Kim *et al.* 2014).

For the flow over a rotating cylinder, numerical simulation has been focused on low Re_D, emphasizing flow instability or vortex shedding at different α. The direct-numerical simulation (DNS) study of Mittal & Kumar (2003) covers $0 \leqslant \alpha \leqslant 5$ at $Re_D = 200$. Vortex shedding is found to shrink with increasing α, disappearing for $\alpha > 1.91$. Another range of one-sided vortex shedding, for $4.34 < \alpha < 4.8$, was also found. Similarly, DNS by Aljure *et al.* (2015) at $Re_D = 5000$ also finds two vortex shedding

ranges. For all cases studied by Aljure *et al.* (2015), turbulent transition occurs in the wake flow and no lift crisis is observed, presumably because Re_D is below Swanson's critical value $Re_D = 3.58 \times 10^4$. The main goal of the present research is to use wall-bounded LES, following Cheng *et al.* (2017, 2018), to investigate the detailed flow physics of the lift crisis at Re_D above this value.

In what follows, the numerical LES method, physical model and the parameter cases considered are described in § 2. In § 3 we consider LES of flows at $Re_D = 6 \times 10^4$ with varying α, showing some surface mean-flow properties such as pressure and skin-friction coefficients. Some LES at relatively low $Re_D = 5 \times 10^3$ are also described as reference flows that do not exhibit the lift crisis. Integrals of wall-surface pressure and skin friction, mainly C_L and the drag coefficient C_D, are compared with existing experimental data, and it is shown that the LES produces a lift crisis at $Re_D = 6 \times 10^4$. In §§ 4 and 5 we utilize diagnostics such as instantaneous surface skin-friction lines, and spanwise-averaged streamlines to elucidate its dynamical underpinnings. This leads to a hypothesis that the lift crisis is the result of flow reorganization characterized by the aggregation of scattered small-scale separation/reattachment cells on the leeward side of the cylinder surface, into a narrow, spanwise band, accompanied by the formation of a corresponding low-pressure spike. Discussion of the flow induced by the rotating cylinder, including incipient turbulence transition behaviour and also the relation between the present lift crisis and the drag crisis in flow over a static cylinder, is given in § 6. Concluding remarks are provided in § 7.

2. Description of LES and cases set-up

2.1. *LES framework: numerical method and physical model*

The governing equations for LES of incompressible viscous flow are derived by formally applying a spatial filter on the Navier–Stokes equations. These are

$$\frac{\partial \widetilde{u}_i}{\partial t} + \frac{\partial \widetilde{u}_i \widetilde{u}_j}{\partial x_j} = -\frac{\partial \widetilde{p}}{\partial x_i} + \nu \frac{\partial^2 \widetilde{u}_i}{\partial x_j^2} - \frac{\partial T_{ij}}{\partial x_j}, \quad \frac{\partial \widetilde{u}_i}{\partial x_i} = 0. \tag{2.1}$$

Here x_i, $i = 1, 2, 3$ are Cartesian coordinates with $\widetilde{u}_i$ the corresponding filtered velocity and $\widetilde{p}$ the filtered pressure. $T_{ij} = \widetilde{u_i u_j} - \widetilde{u}_i \widetilde{u}_j$ denotes the effect of unresolved scales on the resolved-scale motion, which is modelled via a sub-grid scale (SGS) model.

It is convenient sometimes to use (x, y, z) as Cartesian coordinates with (u, v, w) as the corresponding filtered velocity components. Two other coordinate systems are also utilized: the first is cylindrical coordinates (θ, y, r) with velocity components (u_θ, u_y, u_r), which is useful for analysing results, while the second is general curvilinear coordinates (ξ, y, η), used for the implementation of the numerical method.

The governing LES equations are discretized on a body-fitted computational domain (ξ, y, η) which is mapped from the physical domain in (x, y, z) coordinates. Discretization employs a fourth-order-accurate, central-difference scheme for all terms, except the convective term, which uses a fourth-order energy-conservative scheme for the skew-symmetric form (Morinishi *et al.* 1998). For time integration, a third-order Runge–Kutta scheme is used, combined with the fractional-step method. The modified Helmholtz equation for velocity and the Poisson equation for pressure are solved with a multigrid method with line-relaxed Gauss–Seidel smoothers. The code is described in detail by Zhang *et al.* (2015), Zhang & Samtaney (2016) for DNS of airfoil flow and by Cheng *et al.* (2017, 2018) for LES of flow past non-rotating cylinder. The

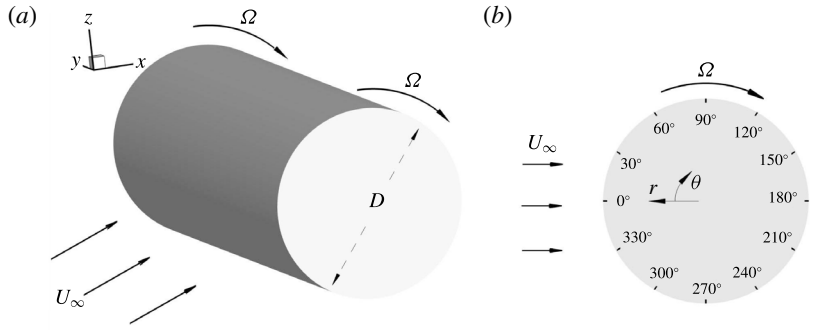

FIGURE 1. Sketch of simulation geometry. (*a*) 3D view of the flow configuration with (x, y, z) coordinates; (*b*) cross-section view of the cylinder with (θ, r) coordinates. θ is measured in the clockwise direction with $\theta = 0$ on the most windward point of the cylinder surface. U_∞ is the free-stream speed and Ω the (constant) angular velocity of the cylinder. The flow can be described by two dimensionless parameters: Reynolds number $Re_D = U_\infty D/\nu$ and velocity ratio $\alpha = \Omega D/(2U_\infty)$, where ν is the kinematic viscosity.

present implementation is identical to that described in § 2.1 of Cheng *et al.* (2017), where outer boundary conditions and use of a sponge region to control the effect of the far wake on the near-cylinder flow are described. All LES reported here use a span-diameter ratio $L_y/D = 3$ and an O grid of radius of $L_r = 40D$. The O grid is a cylinder fitted with equal grid spacing in both the azimuthal and spanwise directions but with grid stretching in the radial direction, particularly near the cylinder surface. The no-slip boundary condition at a stationary cylinder surface is here replaced by $(u_\theta, u_y, u_r) = (\alpha D/2, 0, 0)$ at the cylinder surface.

For LES we employ the stretched-vortex SGS model (SVM) (Misra & Pullin 1997; Voelkl, Pullin & Chan 2000; Chung & Pullin 2009), where the subgrid flow is modelled by spiral vortices (Lundgren 1982) stretched by the eddies comprising the local resolved-scale flow. The implementation of the SVM is described in detail in § 2.2 of Cheng *et al.* (2017, 2018) and summarized presently in appendix B. The surface skin friction is obtained using a one-sided, four-point stencil defined by their equation (2.12) after first subtracting the solid-body rotation field with azimuthal speed αr. The present LES is wall-resolved, meaning that the wall-normal grid size at the wall is on the order of the local viscous wall scale u_τ/ν, where $u_\tau \equiv \sqrt{|\boldsymbol{\tau}_w|/\rho}$ is the friction velocity with $|\boldsymbol{\tau}_w|$ the magnitude of the wall shear stress and ρ the constant fluid density. See Cheng *et al.* (2017) for further details and also tables 1 and 2 of this paper.

2.2. *LES performed*

The cylinder geometry is depicted in figure 1. In (x, y, z) coordinates the free-stream velocity vector is in the positive x-direction while the cylinder axis is aligned with the y-axis. The cylinder rotates with dimensional angular velocity Ω in the sense of the right-hand screw rule. The azimuthal angle θ is as shown. Here and subsequently we refer to that part of the cylinder surface instantaneously lying in $0 \leqslant \theta \leqslant 180°$ $(z \geqslant 0)$, where the x-component of the cylinder surface speed is in the direction of the free stream as the 'top' or advancing part of the cylinder and that part instantaneously in

Case	Re_D	α	N_θ	N_r	N_y	Δr^+
C1	6×10^4	0	512	256	96	0.91
C2	6×10^4	0.2	512	256	96	0.93
C3	6×10^4	0.48	2048	256	192	0.96
F3	6×10^4	0.48	4096	512	384	0.5
C4	6×10^4	0.52	2048	256	192	0.95
C5	6×10^4	0.56	2048	256	192	0.98
C6	6×10^4	0.6	2048	256	192	1.02
F6	6×10^4	0.6	4096	512	384	0.52
C7	6×10^4	0.68	2048	256	192	1.02
C8	6×10^4	0.8	2048	256	192	1.03
C9	6×10^4	1.0	2048	256	192	1.01
C10	6×10^4	2.0	2048	256	192	0.99

TABLE 1. LES flows with $Re_D = 6 \times 10^4$ and varying α. For all cases, the domain size is $40D$ in the radial r direction and $3D$ in the spanwise y direction.

Case	Re_D	α	N_θ	N_r	N_y	Δr^+
A1	5×10^3	0	256	256	64	0.81
A2	5×10^3	0.2	256	256	64	0.82
A3	5×10^3	0.4	256	256	64	0.84
A4	5×10^3	0.6	256	256	64	0.87
A5	5×10^3	0.8	256	256	64	0.85
A6	5×10^3	1.0	256	256	64	0.82
A7	5×10^3	2.0	256	256	64	0.91

TABLE 2. LES flows with $Re_D = 5 \times 10^3$ and varying α. For all cases, the domain size is $40D$ in the radial r direction and $3D$ in the spanwise y direction.

Set	Re_D	α	C_L behaviour	Source
1	5×10^3	0, 1, 2, 3, 4, 5	Increase	Aljure *et al.* (2015)
2	3.58×10^4	$0 \leqslant \alpha \leqslant 1.0$	Flattened increase	Swanson (1961)
3	4.0×10^4	$0 \leqslant \alpha \leqslant 1.0$	Slightly reverse	Takayama & Aoki (2005)
4	4.9×10^4	$0 \leqslant \alpha \leqslant 1.0$	Slightly reverse	Swanson (1961)
5	6.0×10^4	$0 \leqslant \alpha \leqslant 1.0$	Reverse	Takayama & Aoki (2005)
6	6.07×10^4	$0 \leqslant \alpha \leqslant 1.0$	Reverse	Swanson (1961)
7	7.91×10^4	$0 \leqslant \alpha \leqslant 1.0$	Reverse	Swanson (1961)
8	9.9×10^4	$0 \leqslant \alpha \leqslant 1.0$	Reverse	Swanson (1961)
11	1.0×10^5	$0 \leqslant \alpha \leqslant 1.0$	Becomes negative	Takayama & Aoki (2005)
10	1.28×10^5	$0 \leqslant \alpha \leqslant 1.0$	Becomes negative	Swanson (1961)

TABLE 3. Summary of experimental data discussed in the present study.

$180° \leqslant \theta < 360°$ ($z < 0$), where the x-component of the cylinder surface speed opposes the free stream as the 'bottom' or retreating portion of the cylinder surface.

A summary of both experimental and simulation data from reference studies is shown in table 3, with $Re_D \leqslant 1.28 \times 10^5$. For $Re_D = 5 \times 10^3$, DNS results (Aljure *et al.* 2015) show that C_L increases monotonically in the range $0 < \alpha < 5$. In experiments by Swanson (1961), for flows with $3.58 \times 10^4 < Re_D < 4.9 \times 10^4$, the variation of C_L

with α at fixed Re_D does not exhibit a discernible crisis in the sense of a sudden change over a small range of α. For flows with higher Re_D, $C_L(\alpha)$ clearly shows lift crisis behaviour (Swanson 1961; Takayama & Aoki 2005). The experimental data of Takayama & Aoki (2005) show $C_L(\alpha)$ making zero crossings and becoming negative at approximately $Re_D \approx 1.0 \times 10^5$ while the data of Swanson (1961) shows this at $Re_D \approx 1.28 \times 10^5$. Based on the above summary, we choose $Re_D = 5 \times 10^3$ as a starting verification case and also to provide a reference flow behaviour with laminar boundary layers on the cylinder surface. For our main LES we choose $Re_D = 6 \times 10^4$, where the lift crisis has been demonstrated experimentally (Swanson 1961; Takayama & Aoki 2005). Most of our LES utilize $0 \leqslant \alpha \leqslant 1$.

Numerical code verification is described in appendix A. This includes comparison with DNS results at $Re_D = 5 \times 10^3$, analysis of the wall-adjacent mesh size in wall units, examination of the two-point correlation of the spanwise velocity component for evaluating the sufficiency of the chosen spanwise domain, and a mesh refinement study at $Re_D = 6 \times 10^4$ for $\alpha = 0.48$ and $\alpha = 0.6$. Unless otherwise specified, the 'average' or 'mean' is defined as a combined spanwise and time average. The averaging procedure begins after some initial transient period, and spans a time window of 250 units of D/U_∞ for $Re_D = 3.9 \times 10^3$ and approximately 60 times D/U_∞ for $Re_D = 6 \times 10^4$.

3. Cylinder-wall profiles for $Re_D = 6 \times 10^4$ and 5×10^3

3.1. $Re_D = 6 \times 10^4$: *pressure coefficient* C_p *and skin-friction coefficient* $C_{f\theta}$

The LES performed are summarized in table 1. Figure 2 shows azimuthal profiles of the mean surface pressure coefficient $C_p = 2(p - p_\infty)/(\rho U_\infty^2)$ (panels *a*,*c*,*e*,*g*) and the θ component of the mean surface vector skin-friction coefficient $C_{f\theta} = 2\tau_{w,\theta}/(\rho U_\infty^2)$ (panels *b*,*d*,*f*,*h*) for $Re_D = 6 \times 10^4$ over a range of α chosen to capture the expected lift crisis. Here p_∞ is the free-stream pressure which is used to make sure $C_p = 1$ at the front stagnation point. In figure 2(*a*), C_p at $\alpha = 0$ shows symmetric behaviour for the top and bottom parts of the cylinder. As α increases, the azimuthal symmetry about $\theta = 180°$ is broken. At $\alpha = 0.2$, the local minimum C_p for the top portion of the cylinder decreases while the local minimum value on the bottom part of the cylinder increases. This is a natural tendency owing to momentum conservation and should exist for all positive α cases. Similar behaviour is observed for C_p at $\alpha = 0.48$ where the local minimum value on the bottom side of the cylinder has disappeared.

Further increase in α shows a quite different trend, as for example, seen in figure 2(*c*). For $\alpha = 0.52$, a plateau value for C_p has formed which persists with increasing C_p up to $\alpha = 0.56$. At $\alpha = 0.56$ the local minimum on the bottom side has reappeared with a more pronounced negative minimum value compared to the original value at $\alpha = 0$. As α increases further to $\alpha = 0.6$, there is little variation in the C_p profile on the top side of the cylinder, while for the bottom side, a yet deeper valley appears with an even more negative minimum C_p. For larger $\alpha = 0.68, 0.8, 1.0$ shown in figure 2(*e*), the minimum C_p on the top side of the cylinder becomes more negative as α increases while the C_p minimum on the bottom increases algebraically. The plateau value of $C_p \approx -0.7$ remains almost unchanged in this range of α. The overall effect is that C_L again increases with increasing α. At $\alpha = 2$ in figure 2(*g*) the top-side minimum C_p is strongly negative. A C_p plateau still exists but is increased in C_p value and shifted azimuthally towards the bottom surface of the cylinder. There is no local C_p minimum on the bottom side.

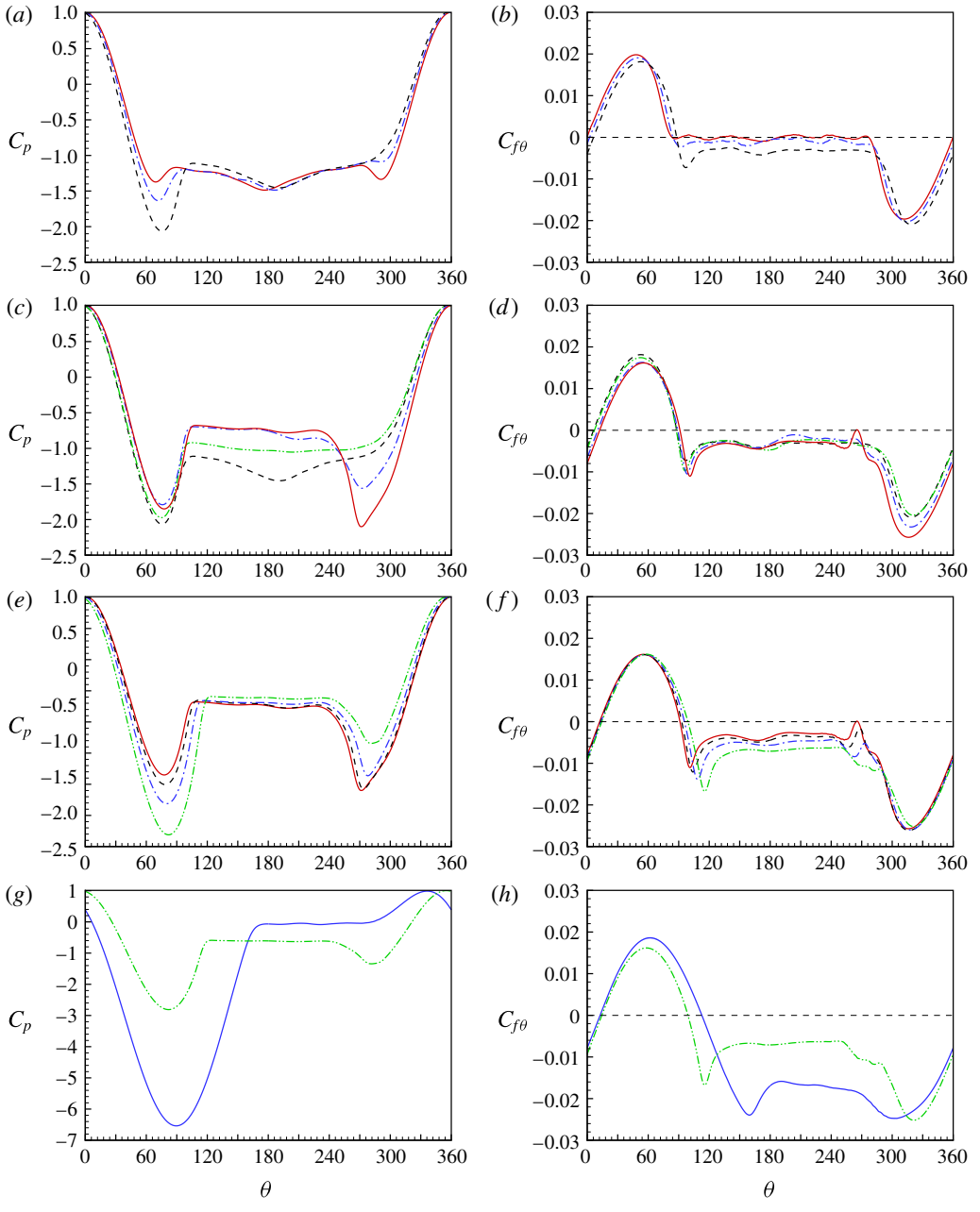

FIGURE 2. (Colour online) $Re_D = 6 \times 10^4$. (*a*,*c*,*e*,*g*) Pressure coefficient C_p. (*b*,*d*,*f*,*h*) Azimuthal component of the skin-friction coefficient $C_{f\theta}$. In (*a*,*b*): ——, $\alpha = 0$; — · —, $\alpha = 0.2$; – – – –, $\alpha = 0.48$. In (*c*,*d*): – – – –, $\alpha = 0.48$, — · · —, $\alpha = 0.52$; — · —, $\alpha = 0.56$; ——, $\alpha = 0.6$. In (*e*,*f*): ——, $\alpha = 0.6$; – – – –, $\alpha = 0.68$; — · —, $\alpha = 0.8$; — · · —, $\alpha = 1.0$. In (*g*,*h*): — · · —, $\alpha = 1.0$; ——, $\alpha = 2.0$.

At $\alpha = 0$, $C_{f\theta}$ is symmetric about $\theta = 180°$ and a small secondary-separation bubble can be observed, as shown in figure 2(*b*). When the cylinder is rotating, the secondary-separation bubble on the top side disappears. For $\alpha > 0.2$, the whole leeward side of

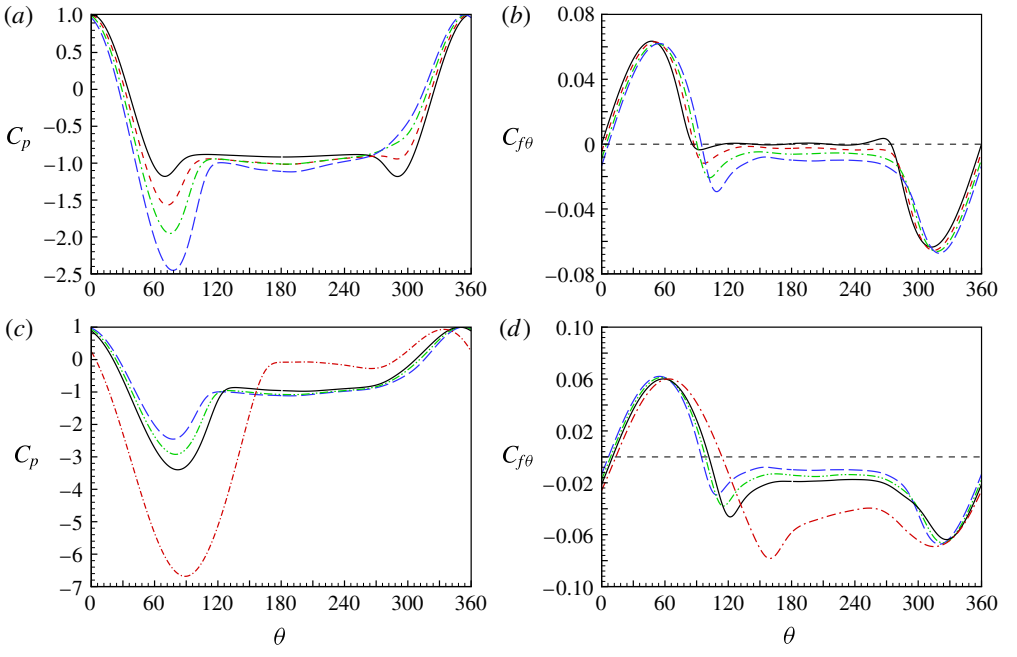

FIGURE 3. (Colour online) C_p and $C_{f\theta}$ at $Re_D = 5 \times 10^3$. (*a*,*c*) C_p; (*b*,*d*) $C_{f\theta}$. In (*a*,*b*): ——, $\alpha = 0$; – – – –, $\alpha = 0.2$; — · —, $\alpha = 0.4$; — — — —, $\alpha = 0.6$. In (*c*,*d*): — — — —, $\alpha = 0.6$; — · · —, $\alpha = 0.8$; ——, $\alpha = 1.0$; — · —, $\alpha = 2.0$.

the cylinder has a negative $C_{f\theta}$ plateau, where a negative value means that the skin-friction force corresponds to a thrust. When $\alpha = 0.48$, this plateau further moves to a lower level at approximately $C_{f\theta} = 0.004$. For $\alpha = 0.48$–0.6 in figure 2(*d*), the plateau $C_{f\theta}$ remains almost constant. At $\alpha = 0.6$, an abrupt hill appears at approximately $\theta = 270°$ and touches $C_{f\theta} = 0$. This implies the incipient appearance of a tiny mean-flow separation region. In figure 2(*f*), further increase of α shows further decrease of the plateau $C_{f\theta}$ value and also a smoothing of the hill. Still further increase to $\alpha = 2.0$, as shown in figure 2(*h*), results in a plateau at a much smaller $C_{f\theta}$.

3.2. $Re_D = 5 \times 10^3$

We discuss LES results at $Re_D = 5 \times 10^3$ as a reference. The LES performed are summarized in table 2. For $Re_D = 5 \times 10^3$, the variation of both C_p and $C_{f\theta}$ with increasing α shows an almost uniform tendency in figure 3. This includes the decreasing minimum C_p on the top side of the cylinder and the gradual disappearance of the minimum C_p on the bottom side. The plateau C_p remains almost unchanged for $\alpha < 1$. The trend of $C_{f\theta}$ variation is similarly uniform, with a monotonically decreasing plateau value.

It is of interest to compare cases with different Re_D at fixed α, for example $\alpha = 2$ in figures 2(*g*,*h*) and 3(*c*,*d*), respectively. Although profiles of $C_{f\theta}$ are rather different, the azimuthal profiles of pressure coefficient are quite close. Both cases have a minimum $C_p \approx -6.5$ near $\theta = 90°$, and also a peak value $C_p \approx 1$ at approximately $\theta = 330°$. Since the pressure distribution on the cylinder surface contributes the dominant part of both the drag and the lift, the dependence of the drag/lift on Re_D is quite weak for high-α cases.

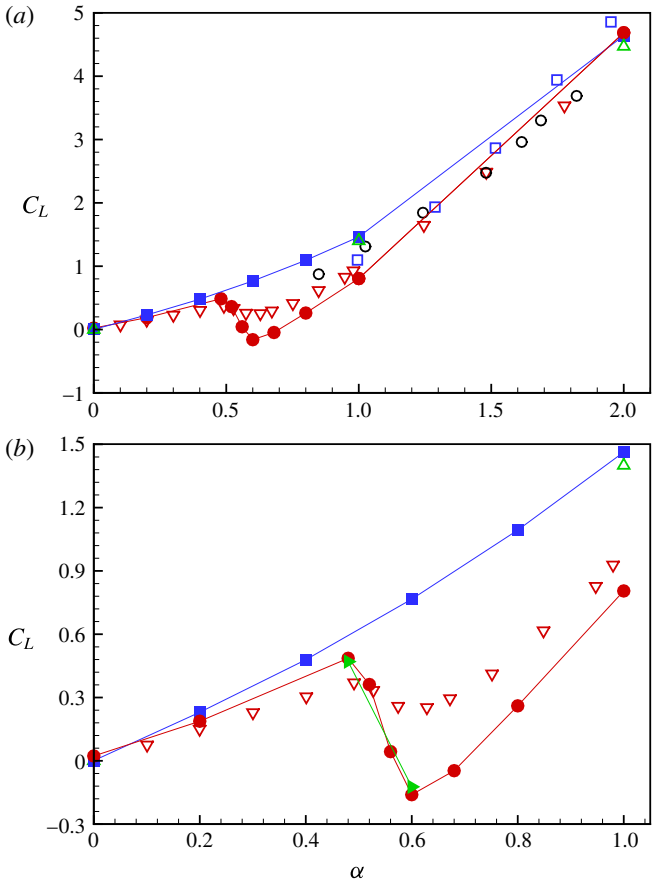

FIGURE 4. (Colour online) Lift coefficient C_L. (*a*) full scale; (*b*) for $0 \leqslant \alpha \leqslant 1$. Present LES data: ■, $Re_D = 5 \times 10^3$; ●, $Re_D = 6 \times 10^4$; ▶, $Re_D = 6 \times 10^4$ with fine mesh. Reference data: △, DNS by Aljure *et al.* (2015) at $Re_D = 5 \times 10^3$; ▽, experiments by Swanson (1961) at $Re_D = 6 \times 10^4$; ○, experiments by Thom (1934) at $Re_D = 5.3 \times 10^3$; □, experiments by Carstensen *et al.* (2014).

3.3. *Lift and drag coefficients C_L, C_D*

It has been seen that the C_p profiles for $Re_D = 6 \times 10^4$ in $0 \leqslant \alpha \leqslant 1$ show rather different features than for $Re_D = 5 \times 10^3$. These account for the presence of the C_L crisis for the higher Re_D and for smaller differences in the $C_D - \alpha$ variation for the two Re_D.

3.3.1. *Lift crisis of $C_L(Re_D, \alpha)$*

The $C_L(Re_D, \alpha)$ results for the present LES are shown in figure 4(*a*) over $0 \leqslant \alpha \leqslant 2$. Here all LES results for $Re_D = 5 \times 10^3$ and 6×10^4 are shown. Also shown are DNS (Aljure *et al.* 2015) at $Re_D = 5 \times 10^3$ and experimental measurements (Thom 1934; Swanson 1961; Carstensen *et al.* 2014). The present LES at $Re_D = 5 \times 10^3$ generally agree with both DNS at the same Re_D and also experiment at $Re_D = 5.3 \times 10^3$ by (Thom 1934). The other two experiments, Swanson (1961), which covers $Re_D = 3.5 \times 10^4$–3×10^5, and Carstensen *et al.* (2014), in the range $Re_D = 3.2 \times 10^4$–9.9×10^4,

agree with each other. Both show a small decrease from measurements at $Re_D = 5 \times 10^3$. This decrease is observed in our LES results with $Re_D = 6 \times 10^4$ at $\alpha = 1$, but not at higher α.

A plot of C_L versus α in $0 \leqslant \alpha \leqslant 1$ is shown in figure 4(*b*). Here LES data at $Re_D = 6 \times 10^4$, with both a fine and coarse mesh, cases 'F' and 'C' respectively of table 1, are included. The former LES are computationally expensive and were performed only at $\alpha = 0.48$, 0.6. They show good agreement with the coarser-mesh LES at these α values, indicating that the coarse-mesh LES are converged. The LES C_L shows reasonable agreement with the data by Swanson (1961) for $\alpha \leqslant 0.48$, before the beginning of the lift crisis. While the range of α spanning the C_L dip is well captured by the LES, the magnitude of the change differs between LES and experiment. In $0.48 \leqslant \alpha \leqslant 0.6$, the experimental data (Swanson 1961) show a decreases $C_L \sim 0.37 \rightarrow 0.24$ whereas LES data from both the fine and coarse-mesh LES show $C_L \sim 0.4 \rightarrow -0.1$. In comparison, Kim *et al.* (2014) report experimental measurements for flow past a rotating sphere showing $C_L \sim 0.3 \rightarrow 0.05$ over the range $\alpha \approx 0.53$–0.7 at the same $Re_D = 6 \times 10^4$. For higher Re_D, up to $Re_D = 1.8 \times 10^5$ they find more negative local C_L minima. The experimental studies by Swanson (1961) and Takayama & Aoki (2005) give scant details of the measurement technique for C_L and so assessment of the experimental accuracy is uncertain. The rotating sphere experiments by Kim *et al.* (2014) show a relatively strong lift crisis consistent with the trend shown by the present LES. We conclude that the magnitude of the lift crisis for a rotating cylinder as a function of (Re_D, α) remains an open question.

3.3.2. *Drag crisis of* $C_D(Re_D, \alpha)$

The drag coefficient results $C_D(Re_D, \alpha)$ are shown in figure 5. In figure 5(*a*), the LES at $Re_D = 5 \times 10^3$ generally agree with DNS by Aljure *et al.* (2015). For this Re_D, the drag decrease is smooth and continuous while for $Re_D = 6 \times 10^4$, C_D shows a somewhat sharp decrease at approximately $\alpha = 0.6$. In figure 5(*b*), we compare the present LES and the experimental data by Swanson (1961) and Takayama & Aoki (2005) at $Re_D = 6 \times 10^4$. The drag crisis is reasonably well captured.

3.3.3. *Time histories of* C_L *and* C_D

The time histories of C_L and C_D for rotating-cylinder flow are known to show regular shedding and a closed curve in a phase diagram of C_L versus C_D, as shown by Mittal & Kumar (2003) for $Re_D = 200$. For high-Reynolds-number flow, strong three-dimensional (3D) flow effects together with turbulent transition in the wake flow are expected to produce a more complex $C_L - C_D$ evolution.

In figure 6, LES results for $\alpha = 0$, 1.0 and 2.0 at $Re_D = 5 \times 10^3$ are shown, including the C_L evolution with time T and also the $C_L - C_D$ phase diagram. Results at $\alpha = 1.0$ show a slight increase of the fluctuation magnitude in $C_L(t)$ compared with $\alpha = 0$, in agreement with the trend of DNS by Aljure *et al.* (2015). At $\alpha = 2.0$, although the vortex shedding should vanish owing to the magnification of the asymmetry, C_L still shows robust oscillatory behaviour owing to turbulence in the far-wake flow. This can also be observed in the $C_L - C_D$ phase diagram, which shows reasonably regular structures corresponding to shedding for $\alpha = 0$ and 1.0, but a rather chaotic trajectory for $\alpha = 2.0$.

In figure 7, results at $Re_D = 6 \times 10^4$ are shown for $\alpha = 0$, 1.0 and 2.0. For this higher Re_D flow, $\alpha = 1.0$ is found to produce a much smaller fluctuation in C_L than for $\alpha = 0$. Also from the phase diagram, $\alpha = 0$ can be seen to produce regular shedding, while for $\alpha = 1.0$ and 2.0, strongly chaotic behaviour overwhelms the shedding and quasiperiodic behaviour is not apparent.

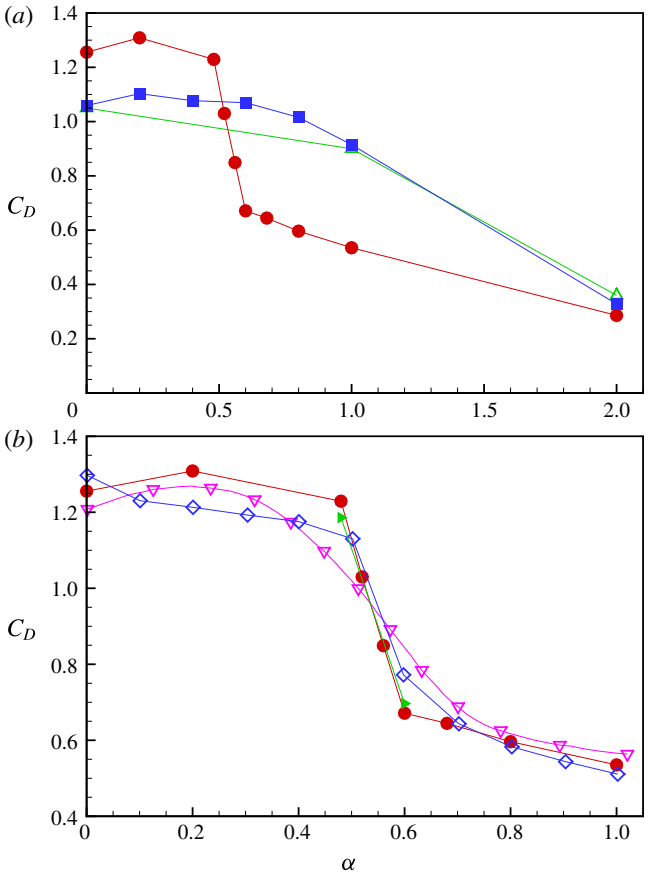

FIGURE 5. (Colour online) Drag coefficient C_D. (*a*) Full scale; (*b*) for $0 \leqslant \alpha \leqslant 1$. Symbols same as in figure 4. ◊, experiments by Takayama & Aoki (2005) at $Re_D = 6 \times 10^4$.

It is of interest to check the time-history behaviour around the lift crisis, for example, $\alpha = 0.48$ before the lift crisis and $\alpha = 0.6$ just following the lift crisis. Figure 8 shows striking differences for these cases. At $\alpha = 0.48$ there is a strong fluctuation in C_L while for $\alpha = 0.6$ this is largely suppressed. This suppression of vortex shedding provides a useful signature of the onset of the lift crisis. In order to quantify the fluctuation behaviour of the lift/drag coefficients we compute the root-mean-square C_{Lrms} and C_{Drms}, of the timewise variation of $C_L(t)$ and $C_D(t)$, respectively. Results for $Re_D = 5 \times 10^3$ are shown in appendix A for comparison with the DNS of Aljure *et al.* (2015). Results at $Re_D = 6 \times 10^4$ are listed in table 4. It can be seen that, after the lift crisis, both C_{Lrms} and C_{Drms} decrease to relatively low values while C_{Lrms} remains nearly constant for $\alpha \geqslant 0.6$.

4. Skin-friction portraits and mean-flow streamlines

4.1. *Flow reorganization: the instantaneous* $\boldsymbol{C_f}$ *vector field*

Following Cheng *et al.* (2017), we discuss separation and reattachment events as flow near or surrounding critical points of the $\boldsymbol{C_f}$ vector field on the cylinder surface.

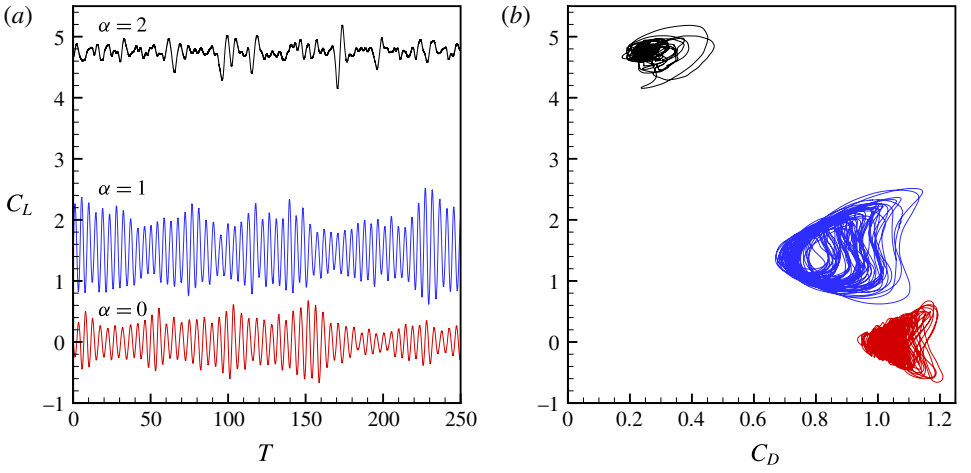

FIGURE 6. (Colour online) C_L and C_D for $Re_D = 5 \times 10^3$, cases: $\alpha = 0, 1.0, 2.0$. (*a*) Time histories of $C_L(T)$, where $T = tU_\infty/D$ is dimensionless physical time. (*b*) C_L–C_D phase diagram.

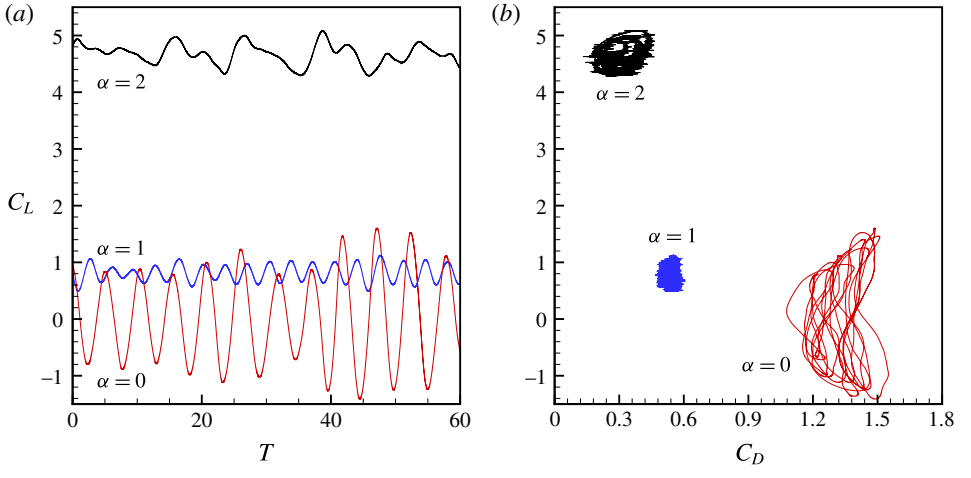

FIGURE 7. (Colour online) C_L and C_D for $Re_D = 6 \times 10^4$, $\alpha = 0, 1.0, 2.0$. (*a*) Time histories of C_L. (*b*) C_L–C_D phase diagram.

α	0.0	0.2	0.48	0.52	0.56	0.6	0.68	0.8	1.0	2.0
C_{Lrms}	0.77	0.79	0.88	0.34	0.15	0.17	0.18	0.18	0.17	0.18
C_{Drms}	0.12	0.13	0.15	0.041	0.037	0.027	0.031	0.016	0.028	0.066

TABLE 4. LES calculation of lift coefficient fluctuation C_{Lrms}, and drag coefficient fluctuation C_{Drms}: $Re_D = 6 \times 10^4$.

Two representative $\boldsymbol{C}_f$ surface fields for $Re_D = 6 \times 10^4$ are shown in figure 9 for $\alpha = 0.48$ and $\alpha = 0.6$. With $\alpha = 0.48$, the flow attachment line, indicated by diverging $\boldsymbol{C}_f$ trajectories, is seen at approximately $\theta = 5°$. On the top side of the cylinder, the

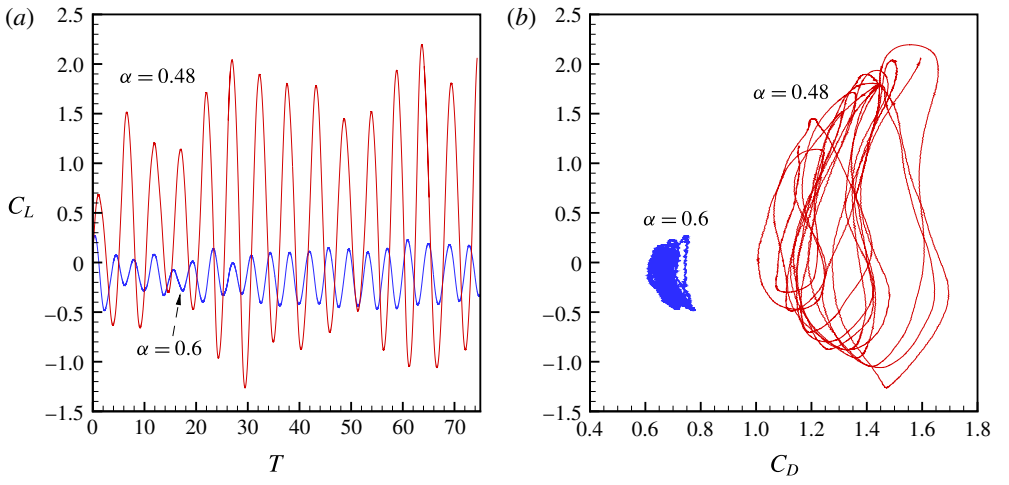

FIGURE 8. (Colour online) C_L and C_D for $Re_D = 6 \times 10^4$ across the lift crisis: $\alpha = 0.48, 0.6$. (*a*) Time histories of C_L. (*b*) C_L–C_D phase diagram.

attached flow shows large-scale separation at approximately $\theta = 96°$ while on the bottom side, the attached flow does not show a focused separation line. According to Chong *et al.* (1998), prior to the main flow separation, there generally exists fluctuating small-scale flow reversals scattered over a finite portion of the body surface, corresponding to multiple, scattered critical points in the $\boldsymbol{C}_f$ field. For $\alpha = 0.48$, for example at $y/D = 1.0$, the flow shows critical points at approximately $\theta = 264°$ while at $y/D = 2.5$, these are present at approximately $\theta = 216°$. This indicates that the flow is locally strongly 3D and unsteady, with the consequence that structured separation is difficult to recognize.

In contrast, with $\alpha = 0.6$, the $\boldsymbol{C}_f$ surface field shows a somewhat different appearance. The attachment stagnation line moves to approximately $\theta = 12°$, while the separation line on the top side of the cylinder is still at around $\theta = 96°$. Near $\theta = 270°$ the flow on the bottom side of the cylinder forms small-scale reversal flow cells concentrated in a zone $\theta \approx 250°$–$280°$ and extending across the entire span. A close-up view in $0 < y/D < 0.4$ is shown in figure 10. Localized flow reversals correspond to bundles of skin-friction lines appearing as separatrices connecting critical points of the $\boldsymbol{C}_f$ field. Example critical points are labelled as 'repelling' (square symbol), where skin-friction lines diverge indicating localized reattaching flow, and as 'attracting' (circular symbol), where skin-friction converge implying local flow separation. A large array of roughly randomly distributed critical points exists in this region at the time instant displayed. We refer to this as an aggregation zone of small-scale, flow separation/reattachment cells. Its formation is interpreted as strong evidence of structured but distributed localized flow separation/reattachment.

4.2. *Sequential* $\boldsymbol{C}_f(\theta, y)$ *portraits*

In figure 11 we show the instantaneous lift coefficient $\boldsymbol{C}_f(\theta, y)$ at several different times during a cycle for $\alpha = 0.48$ and 0.6 at $Re_D = 6 \times 10^4$. In each panel we mark four dots which represent times at which the instantaneous C_f fields are plotted. For the four points, point A is close to $C_L = 0$, point B corresponds to minimum C_L, point C is near the midvalue between the valley and peak and point D is around the C_L

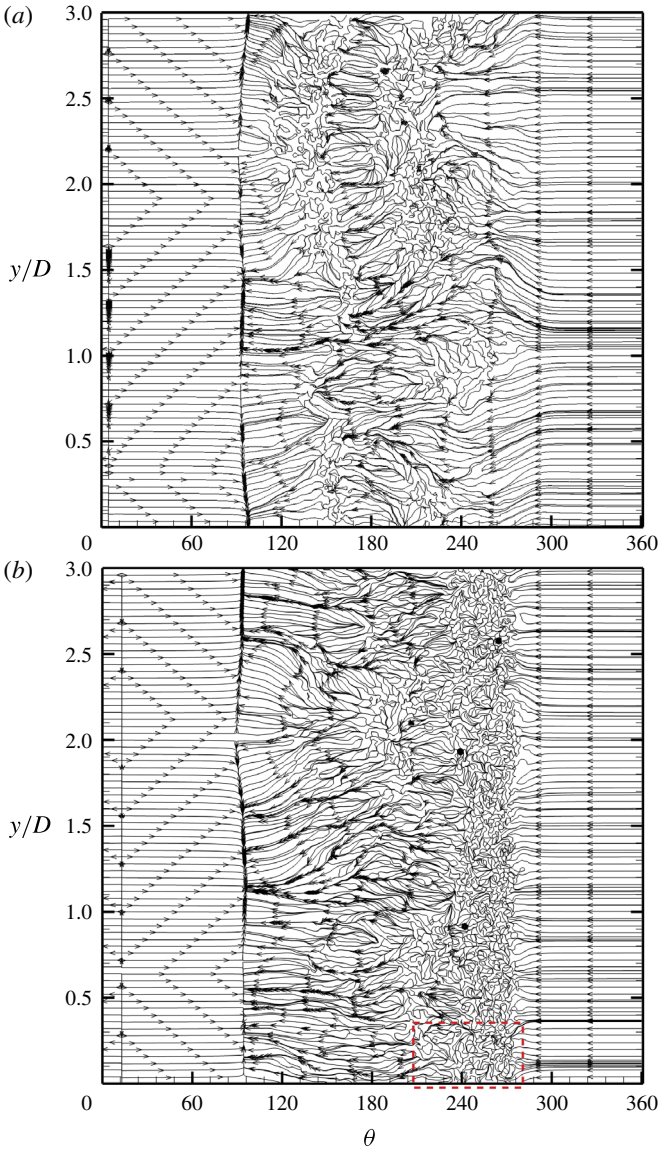

FIGURE 9. (Colour online) Skin-friction lines for case at $Re_D = 6 \times 10^4$. (*a*) $\alpha = 0.48$; (*b*) $\alpha = 0.6$.

peak. For $\alpha = 0.48$, two other instants labelled as C′ and D′ are shown, which will be discussed subsequently.

4.2.1. $\alpha = 0.48$

For $\alpha = 0.48$, we emphasize again that the flow on the bottom cylinder surface does not clearly show a structured pattern in the range $\theta = 200°$–$270°$ due to its strong flow variation in the spanwise direction. In figure 12, at instant B the whole skin-friction field looks chaotic with no obvious unidirectional flow apparent at approximately $\theta = 180°$, while for instant C a clockwise wash flow is evident at approximately

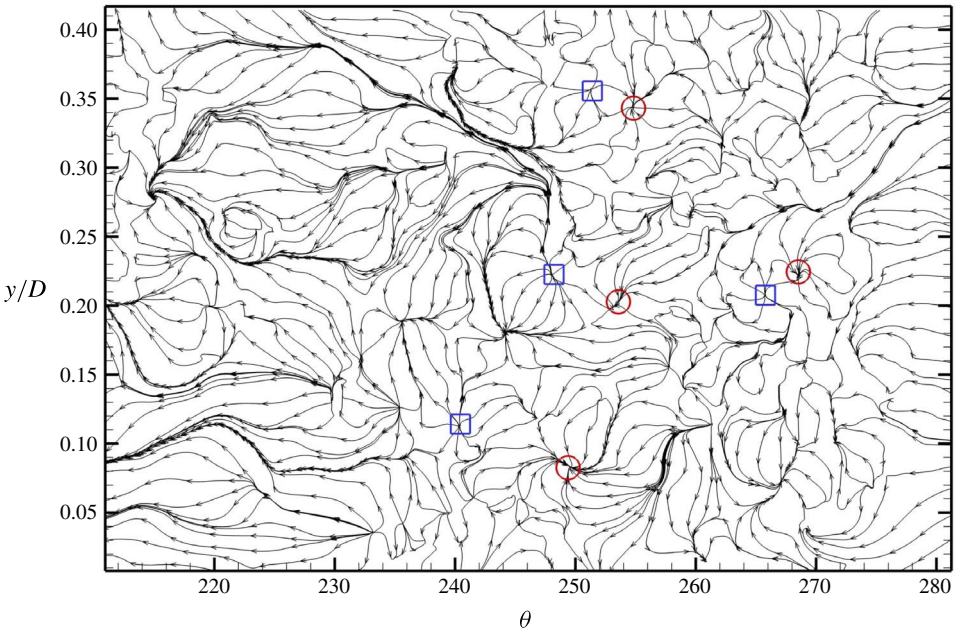

FIGURE 10. (Colour online) Skin-friction lines for case at $Re_D = 6 \times 10^4$ and $\alpha = 0.6$. This shows a close-up view of the band of small-scale separation/reattachment cells. □, typical repelling points (local flow reattachment). ○, typical attracting points (local flow separation).

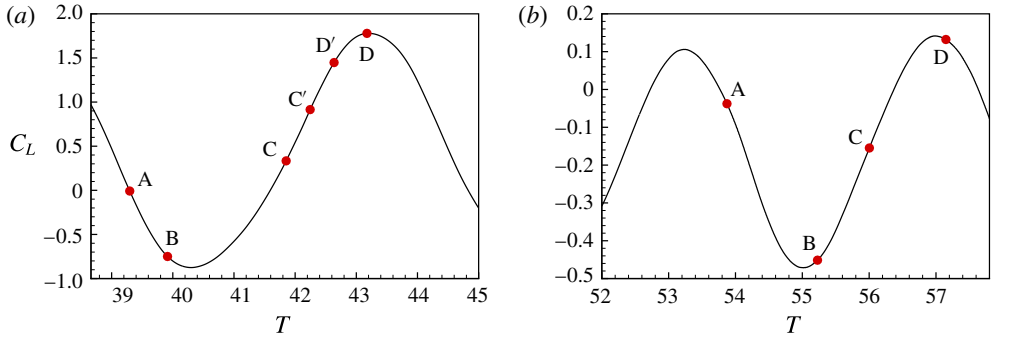

FIGURE 11. (Colour online) C_L versus time for cases at $Re_D = 6 \times 10^4$. (*a*) $\alpha = 0.48$; (*b*) $\alpha = 0.6$. Points labelled A, B, C and D are used for comparison of flow behaviour in the shedding process. Points labelled C′ and D′ at $\alpha = 0.48$ are useful intermediate points.

$\theta = 180°$. Among the four plots, the instant D, where C_L shows a maximum, shows strong anticlockwise wash flow towards the top side of the cylinder at around 180°. The nomenclature 'wash flow' is presently used to denote a sloshing and reversing but largely attached surface flow. To clarify, in figure 13, we show close-up views at instants C and D for $1.5 < y/D < 2.0$. At around $\theta = 180°$, footprints of attached clockwise directional attached flow are clearly visible at C, while at instant D, anticlockwise flow is evident. The existence of wash flow, which implies visible vortex shedding, is a feature of the flow at $\alpha = 0.48$.

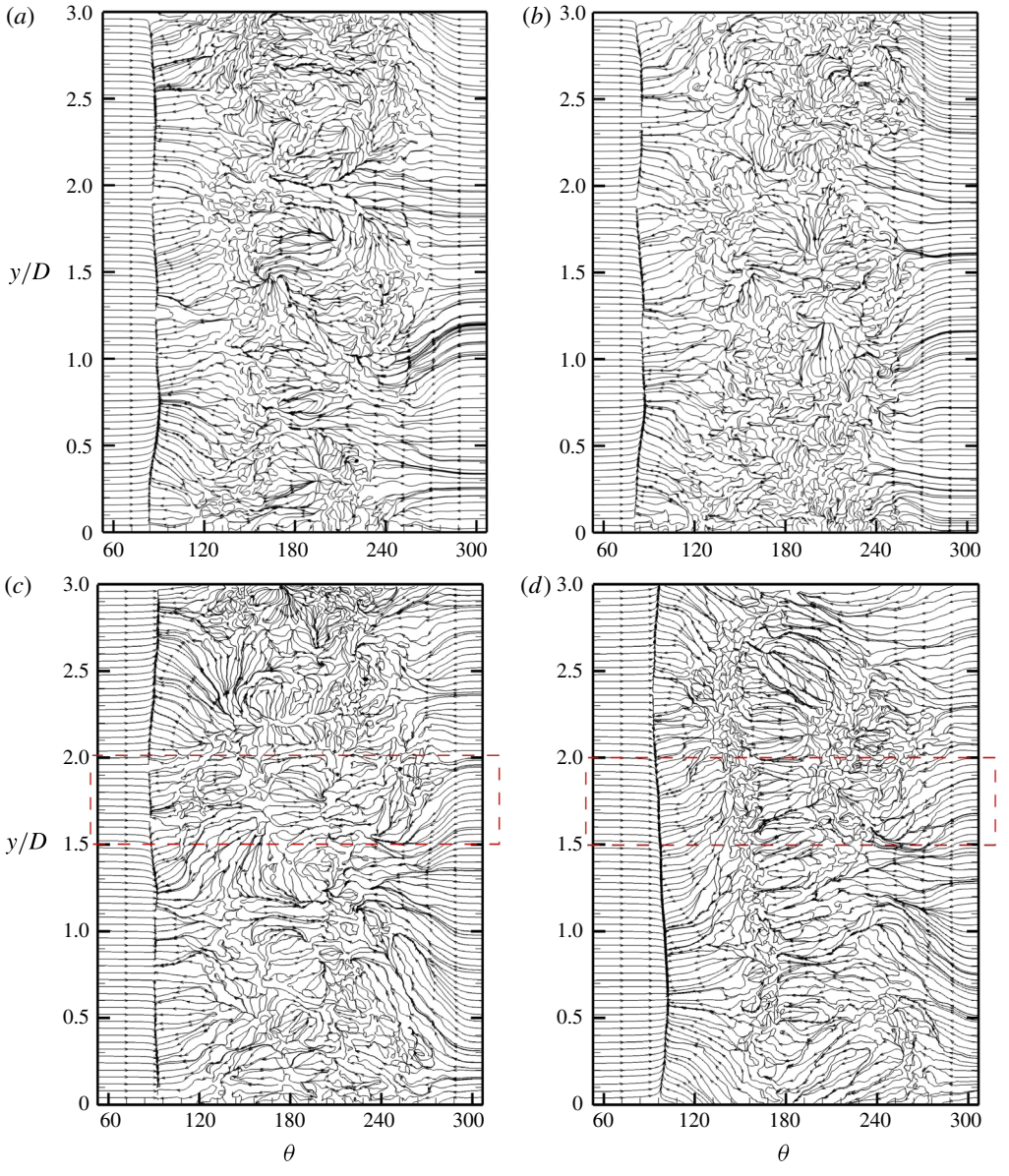

FIGURE 12. (Colour online) Instantaneous skin-friction lines for $\alpha = 0.48$ at $Re_D = 6 \times 10^4$. (*a*) Instant A; (*b*) instant B; (*c*) instant C; (*d*) instant D. For the corresponding C_L for each instant, see figure 11(*a*).

The directional change of the wash flow provides evidence of some quasiperiodic flow behaviour. To explore this we implement a spanwise average for the four instantaneous flow fields, and plot their streamlines in figure 14. If $\boldsymbol{u}(\theta, y, r, t)$ represents the full velocity field, we define spanwise-averaged, instantaneous streamlines of the modified field $\boldsymbol{u}_\alpha = (u_{\alpha,\theta}, u_{\alpha,y}, u_{\alpha,r})$

$$\boldsymbol{u}_\alpha(\theta, y, r, t) \equiv \boldsymbol{u}(\theta, y, r, t) - \alpha r \boldsymbol{e}_\theta. \tag{4.1}$$

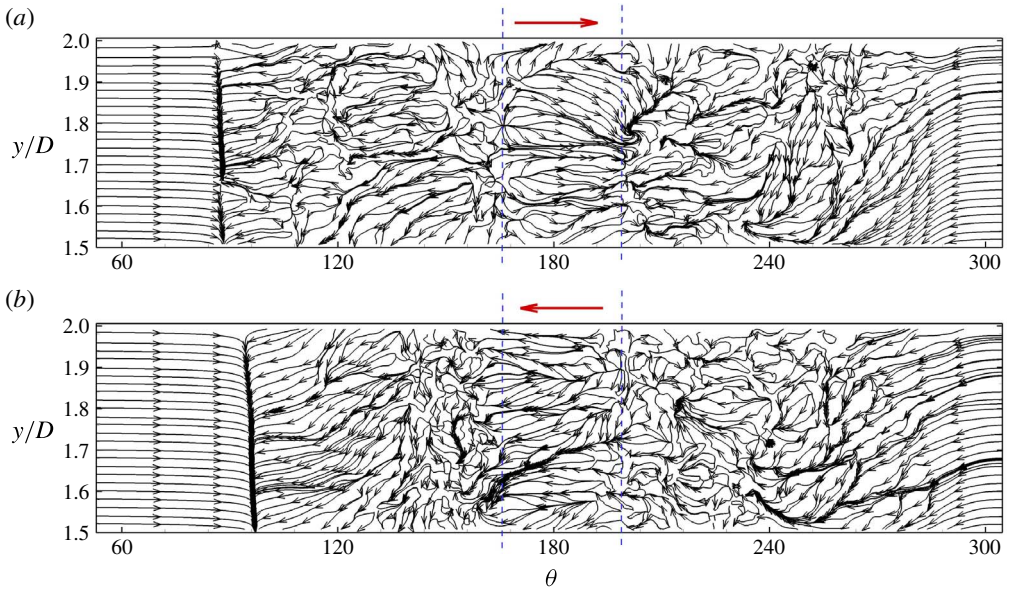

FIGURE 13. (Colour online) Examples of 'wash flow' in instantaneous skin-friction lines for $\alpha = 0.48$ at $Re_D = 6 \times 10^4$. (*a*) Close-up at instant C; (*b*) close-up at instant D.

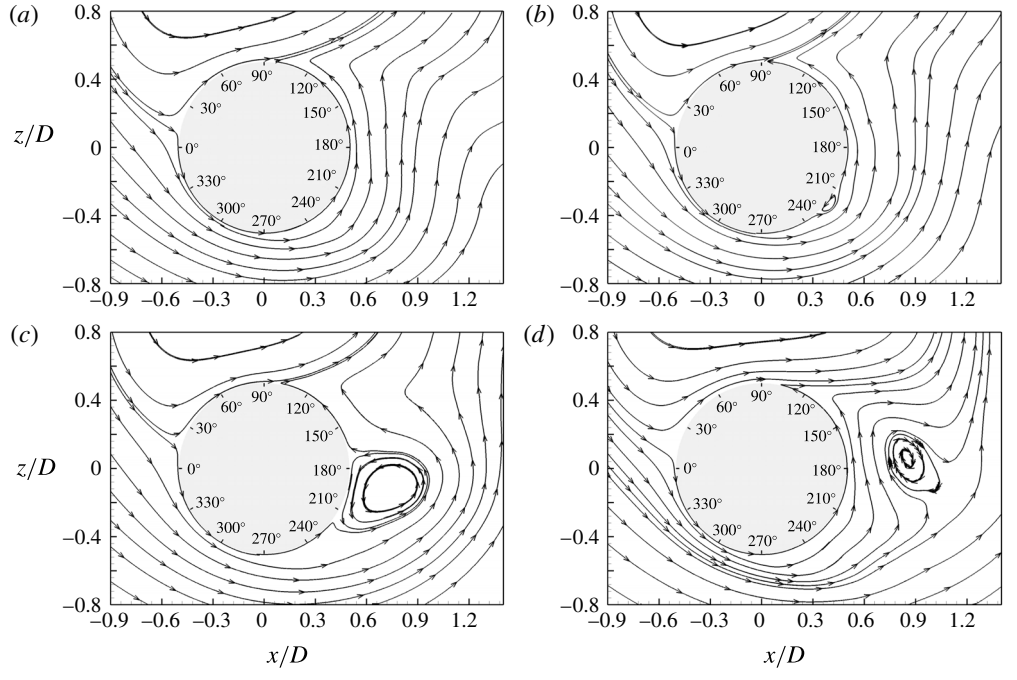

FIGURE 14. Streamlines of instantaneous spanwise-averaged fields of $\boldsymbol{u}_\alpha(\theta, y, r, t)$ (defined in (4.1)) for $\alpha = 0.48$ at $Re_D = 6 \times 10^4$. (*a*) Instant A; (*b*) instant B; (*c*) instant C; (*d*) instant D. For the corresponding C_L for each instant, see figure 11(*a*).

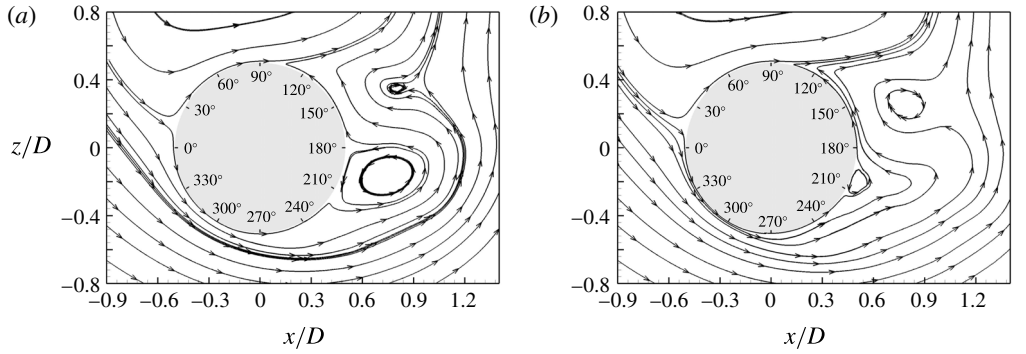

FIGURE 15. Streamlines of instantaneous spanwise-averaged fields of $\boldsymbol{u}_\alpha(\theta, y, r, t)$ (defined in (4.1)) for $\alpha = 0.48$ at $Re_D = 6 \times 10^4$. (*a*) instant C′; (*b*) instant D′.

This is used because $\boldsymbol{u}_\alpha(\theta, y, r, t) = 0$ on the cylinder surface, and, as a consequence, the $\boldsymbol{C}_f$ portraits are in fact the limiting streamlines of $\boldsymbol{u}_\alpha(\theta, y, r \to D/2, t)$ on the cylinder surface, and not of $\boldsymbol{u}(\theta, y, r \to D/2, t)$. In fact this can be formulated as a general principle for bodies that are heaving and rotating with respect to a fixed laboratory frame of reference. For instant A, the streamlines clearly show two flow regions. On the top of the cylinder, the flow attaches at approximately $\theta = 10°$ and separates at approximately $\theta = 100°$. On the cylinder bottom, the flow is also attached at approximately 10° and separates at approximately 100°. For instant B a small separation bubble appears in the range of $210° < \theta < 230°$, which corresponds to strongly 3D skin-friction lines. For instant C, this anticlockwise separation bubble increases, reflecting the strong clockwise directional wash flow evident in the skin-friction lines plot. For instant D, the near-wall flow on the bottom side of the cylinder is again fully attached, while downstream there is a clockwise-rotating vortex.

To expose detailed differences between instants C and D, we show further streamline patterns in figure 15. Figure 15(*a*), which corresponds to instant C′, shows a clockwise vortex at approximately $\theta = 150°$, located off the wall and within the flow, induced by the strong shear layer. With further development, in figure 15(*b*) which corresponds to instant D′, we find that the wall-attached separation bubble shrinks while the new clockwise vortex increases in extent. This flow behaviour is further followed by instant D (figure 14*d*), where the separation bubble disappears. This process provides a full sequence consisting of the appearance/disappearance of a pair of vortices, one anticlockwise and attached to the wall, and the other clockwise and off the wall.

4.2.2. $\alpha = 0.6$

The four snapshot fields in figure 16 for $\alpha = 0.6$ look more ordered in the sense of a broad spanwise coherent region of anticlockwise near-surface flow. For the flow on the bottom side of the cylinder, all fields show a spanwise band of small-scale separation/reattachment cells restricted to the range $\theta = 250°$–$280°$. For instants A, C and D, this small-scale, flow-reversal region extends approximately 30° and, at $\theta = 180°$, unidirectional wash flow can be seen. For instant B, which corresponds to the C_L minimum, this region extends across a large range, reaching beyond $\theta = 180°$. For all time instants, the centre of this small-scale separation/reattachment zone corresponds

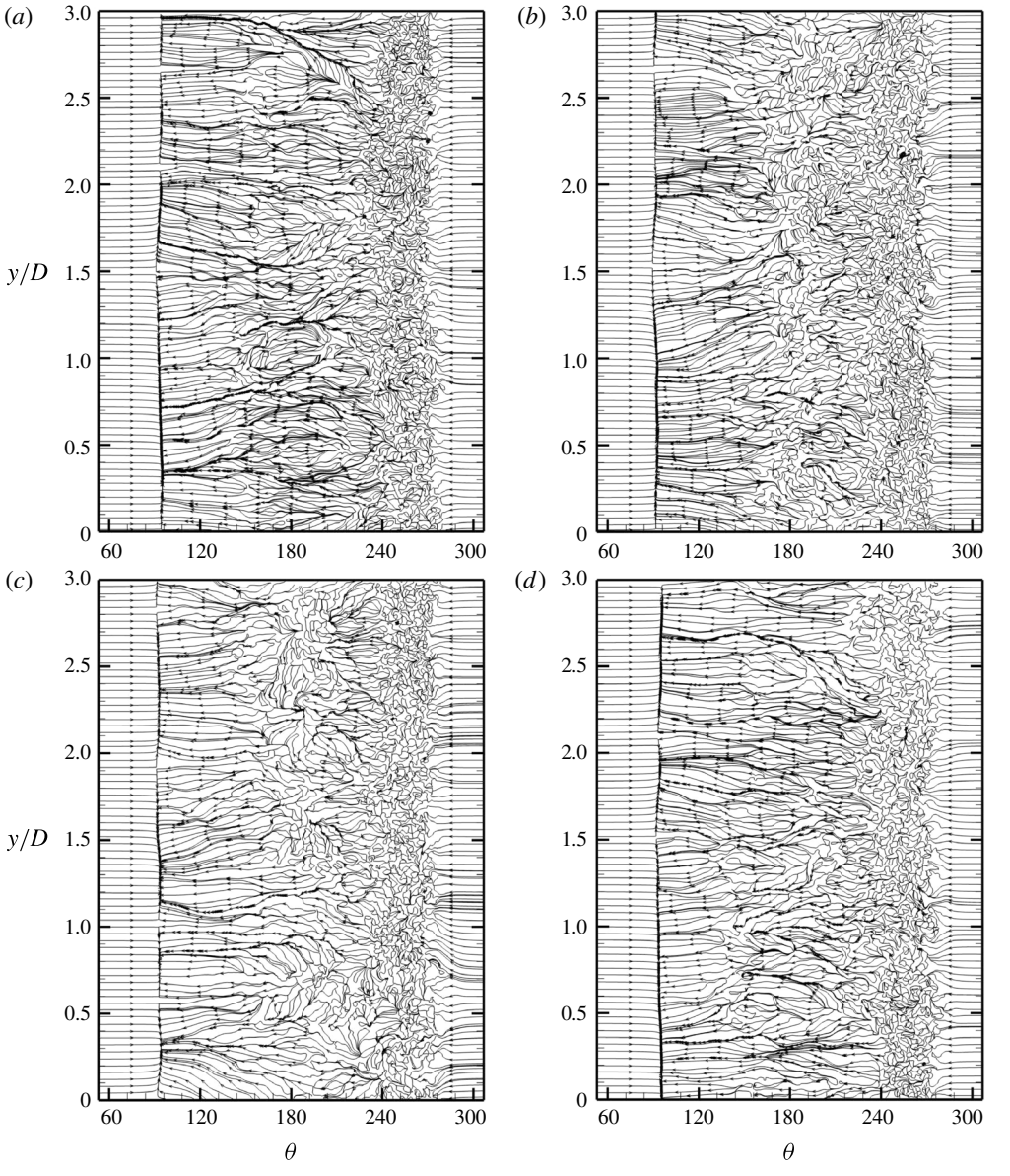

FIGURE 16. Instantaneous skin-friction lines for $\alpha = 0.6$ at $Re_D = 6 \times 10^4$. (*a*) Instant A; (*b*) instant B; (*c*) instant C; (*d*) instant D. For the corresponding C_L for each instant, see figure 11(*b*).

to the θ-location of the pressure minimum of figure 2(*c*,*e*), and is thus associated with the sudden drop in C_L, or the lift crisis. No obvious wash flow can be found in any cases. The streamlines for the spanwise-averaged, instantaneous fields are plotted in figure 17. In each of the four cases, the flow on the bottom side of the cylinder does not show any coherent separation bubble phenomena. This indicates that the small-scale reversal flow field in the band $\theta = 240°$–$280°$ does not produce strong, large-scale vortex shedding.

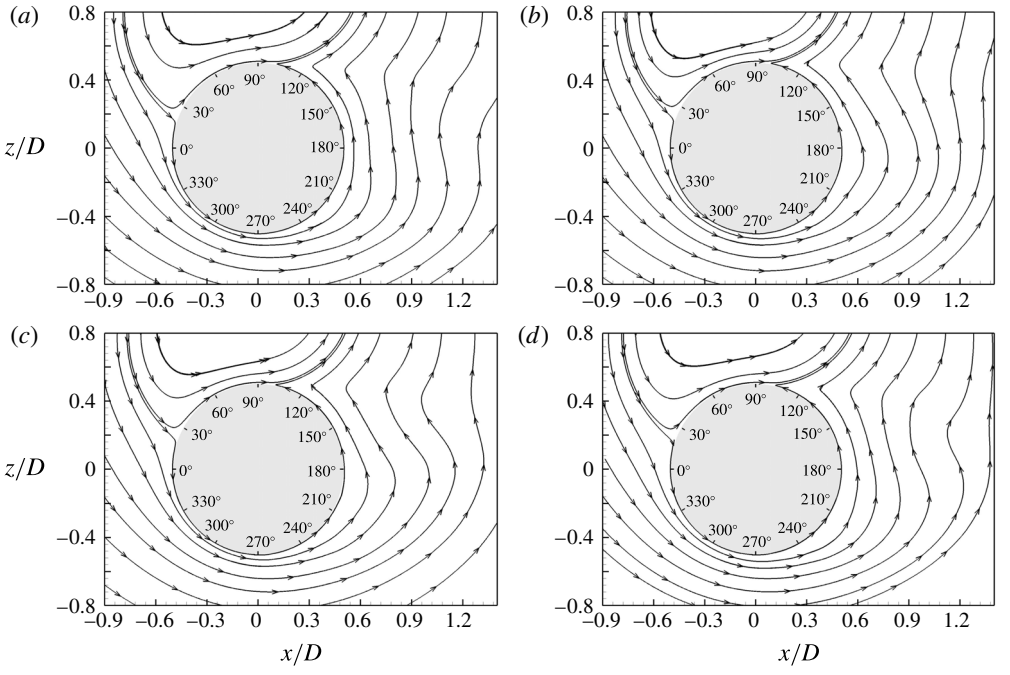

FIGURE 17. Streamlines of instantaneous spanwise-averaged fields of $\boldsymbol{u}_\alpha(\theta, y, r, t)$ (defined in equation (4.1) for $\alpha = 0.6$ at $Re_D = 6 \times 10^4$. (*a*) Instant A; (*b*) instant B; (*c*) instant C; (*d*) instant D. For the corresponding C_L for each instant, see figure 11(*b*).

The flow differences between $\alpha = 0.48$ and $\alpha = 0.6$ can also be seen in figure 18, which shows colour-coded instantaneous but spanwise-averaged vorticity fields with spanwise-averaged streamlines imposed at instant C. Clear vortex formation can be observed for $\alpha = 0.48$, while little large-scale coherent vortex shedding is observed for $\alpha = 0.6$. For $\alpha = 0.6$, a high vorticity region forms around the bottom of the cylinder. This is a signature of local dynamic recirculation flow, which is part of the separation phenomenon. A 3D view of this vorticity distribution is provided in figure 19, which clearly shows the near-wall thin layer containing strong vorticity.

4.2.3. $\alpha = 1,\ \alpha = 2$

Since we hypothesize that the flow reorganization is characterized by the aggregation of the small-scale separation/reattachment events, it is prudent to check the behaviour of the $\boldsymbol{C}_f$ field for higher-α cases. In figure 20, we show two plots of the skin-friction lines at $Re_D = 6 \times 10^4$ for $\alpha = 1$ corresponding to minimum and maximum C_L during a cycle. Little difference can be seen between the plots. A notable feature is the shrinking of the azimuthal extent of the small-scale separation/reattachment cell zone, which for $\alpha = 0.6$ typically spans a range of approximately 30°, and approximately 15° for $\alpha = 1$. At $\alpha = 2$ in figure 21, small-scale reversal flows can barely be seen at around $\theta = 270°$ and most of the skin-friction lines are continuous on the entire surface without critical points, except on the reattachment line at approximately 15° and on the separation line at approximately 115°.

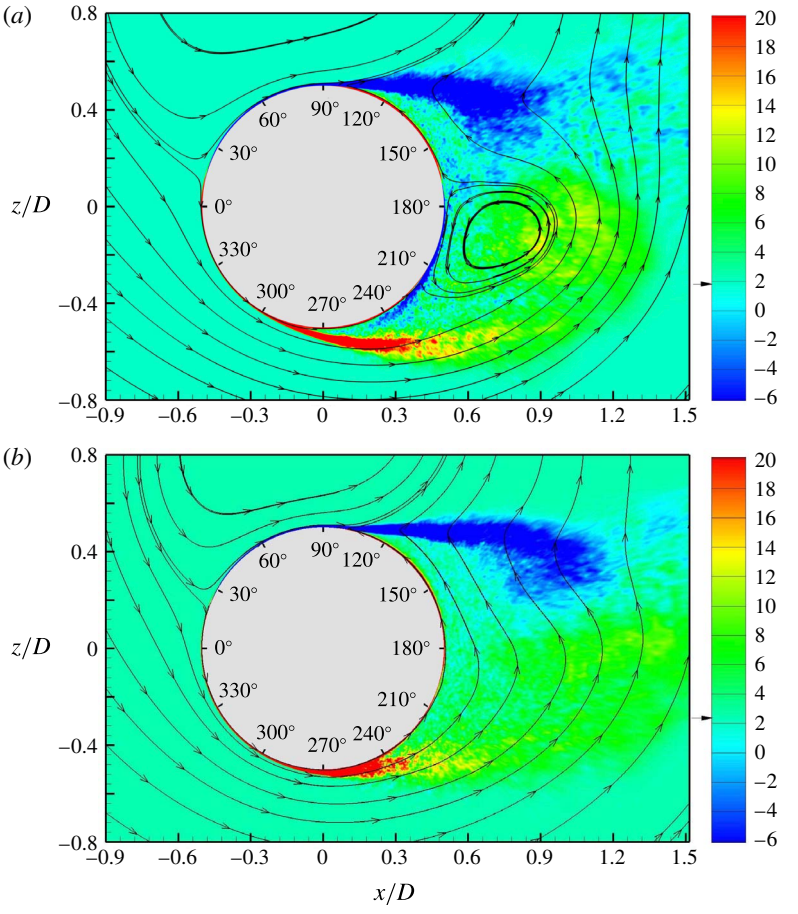

FIGURE 18. (Colour online) Instantaneous, spanwise-averaged spanwise vorticity for $Re_D = 6 \times 10^4$ at instant of 'C' corresponding to figures 14(*c*) and 17(*c*). (*a*) $\alpha = 0.48$; (*b*) $\alpha = 0.6$. The arrow near the colour bar indicates the ambient vorticity $\omega_\infty = 4\alpha U_\infty/D$: $\omega_\infty = 1.92$ for (*a*), $\omega_\infty = 2.4$ for (*b*).

4.3. *Instantaneous pressure field*

The changes in skin-friction portraits between $\alpha = 0.48$ and $\alpha = 0.6$ suggest examination of the corresponding pressure distribution on the cylinder surface. In figure 22, we show colour-coded maps of the surface pressure for $\alpha = 0.48$, 0.6 and 1.0. These show substantial changes in the location of the low-pressure region on the cylinder bottom as α increases at fixed Re_D. A low-pressure region appears at approximately $\theta = 200°$ for $\alpha = 0.48$, shifting to around $\theta = 270°$ for $\alpha = 0.6$. This clearly shows the flow separation behaviour across the lift crisis. For $\alpha = 1.0$, the relative low-pressure region on the bottom part of the cylinder still resides around $\theta = 270°$ but is much weaker than for $\alpha = 0.6$. A large low-pressure region can be seen on the top side of the cylinder. This is a common feature at all Re_D with increasing α.

A close-up view in figure 23 illustrates the relation between instantaneous pressure and identifiable features of the surface skin-friction portrait. The converging separatrices are indicative of locally separating flow, and can be seen to correspond

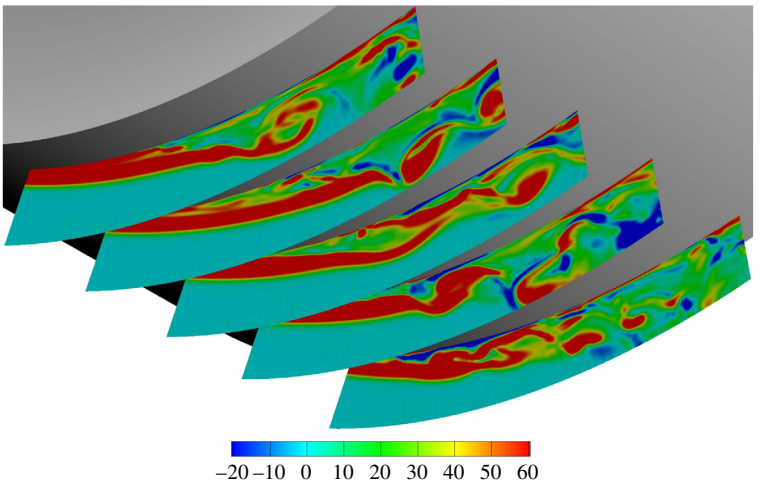

FIGURE 19. (Colour online) An instantaneous spanwise vorticity field for $\alpha = 0.6$ at several spanwise slices.

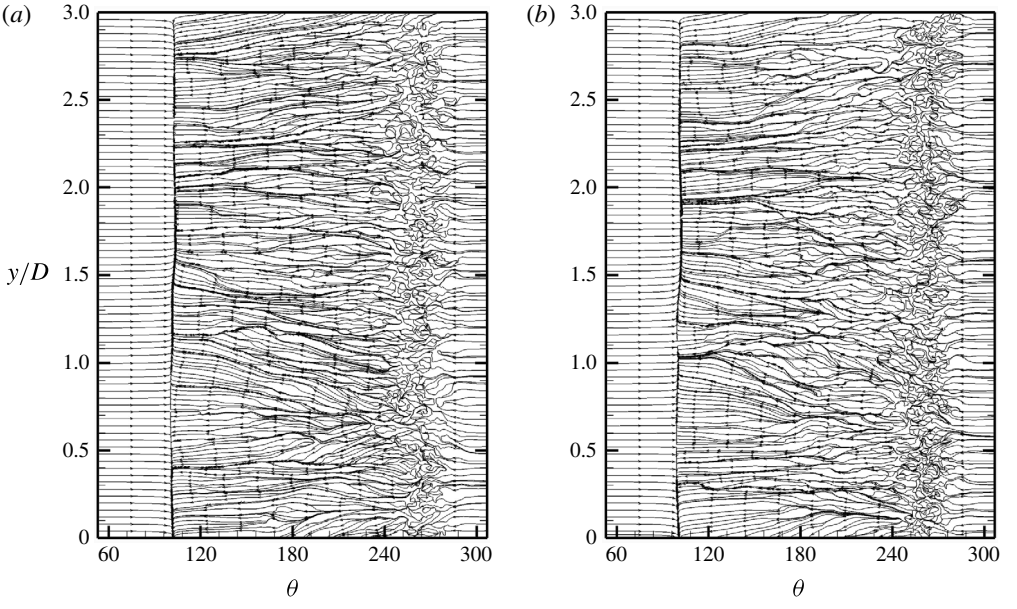

FIGURE 20. Skin-friction lines for $Re_D = 6 \times 10^4$ and $\alpha = 1.0$. (*a*) Instant with minimal C_L; (*b*) instant with maximum C_L.

to local, instantaneous minimal pressure, while the diverging bundles of skin-friction lines, associated with flow reattachment, tend to accumulate on patches of local maximum pressure. According to this correspondence between small-scale separation/reattachment zones, as seen in the surface skin-friction portrait, and local minima/maxima in pressure, it is reasonable to conclude that the formation of small-scale structures, perhaps in the form of near-wall recirculation eddies, results

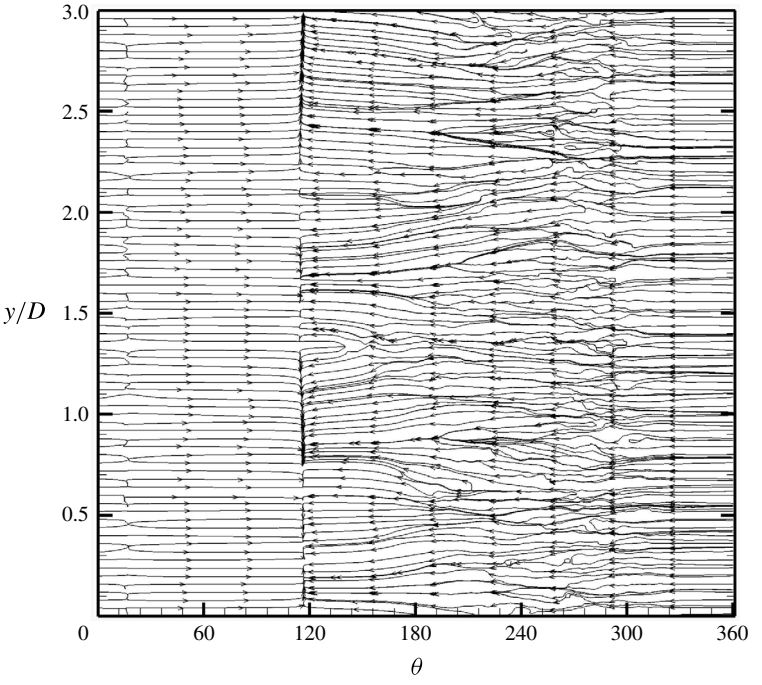

FIGURE 21. Skin-friction lines for $Re_D = 6 \times 10^4$ and $\alpha = 2.0$.

in local separation/reattachment behaviour. This is also apparent in the thin, near-wall region with concentrated vorticity, as shown in figure 19.

4.4. *Mean flow*

In the above comparison of surface skin-friction images for cases before ($\alpha = 0.48$) and after ($\alpha = 0.6$) the lift crisis, we examine features of the instantaneous, spanwise-averaged flow field in order to examine local flow detail, revealing complex vortex movement for $\alpha = 0.48$ but relatively smooth flow for $\alpha = 0.6$ and above. Here we give a short description of streamlines of the mean flow at $Re_D = 6 \times 10^4$, defined as a time–spanwise-averaged flow. In figure 24(*a*,*b*), we show the streamlines of the mean $\boldsymbol{u}_\alpha(\theta, y, r, t)$ velocity field where the two cases shows similar streamlines, all attached on the wall except for the windward attachment at around 15° and separation at approximately $\theta = 96°$. In figure 24(*c*,*d*), we plot the streamlines of the mean $\boldsymbol{u}(\theta, y, r, t)$ field. The clockwise-rotating vortex bubbles in the plots should not be considered as separation bubbles. Because the cylinder is rotating, the near-wall flow always follows the wall movement and thus the clockwise vortex, which has a near-wall reversed direction, cannot reside on the surface. The flow is also characterized by an anticlockwise wall-attached bubble and an off-wall vortex. However, since we are observing the structure in the laboratory-frame velocity field, $\alpha = 0.48$ shows a smaller vortex size which extends to only $x/D \approx 0.8$ while $\alpha = 0.6$ shows a larger scale vortex which extends to $x/D \approx 1.3$. A further detail is that, for $\alpha = 0.6$, at around $\theta = 270°$, the $\boldsymbol{u}(\theta, y, r, t)$ flow shows a small bubble, which although still part of the wall-attached bubble, has its own low-pressure region. This is exactly the flow signature of the low-C_p region, and in fact corresponds to the aggregation of the small-scale separation/reattachment cells on the wall discussed earlier.

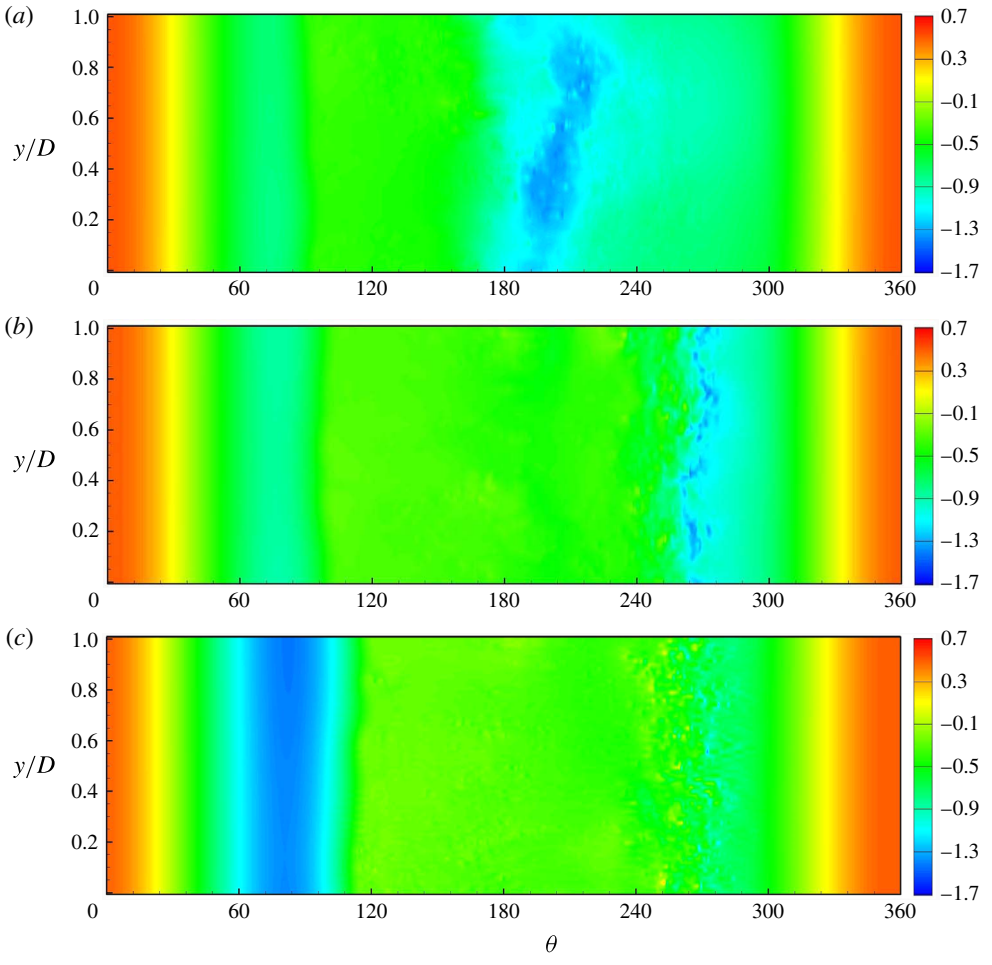

FIGURE 22. (Colour online) Instantaneous pressure field on the cylinder surface for $Re_D = 6 \times 10^4$. (*a*) $\alpha = 0.48$; (*b*) $\alpha = 0.6$; (*c*) $\alpha = 1.0$.

5. Statistical diagnostics of skin-friction vector field C_f

5.1. *PDF of skin-friction coefficient* $C_{f\theta}$

To quantify the statistical features of the $C_{f\theta}$ profile, we sort $C_{f\theta}(y, t)$ over a long time frame and so construct the joint probability distribution function (PDF) $P(C_{f\theta}, \theta)$, normalized such that

$$\int_{-\infty}^{\infty} P(C_{f\theta}, \theta)\, \mathrm{d}C_{f\theta} = 1. \tag{5.1}$$

Scatter plots depicting $P(C_{f\theta}, \theta)$ at $Re_D = 6 \times 10^4$, with $\alpha = 0.48$ and $\alpha = 0.6$, are shown in figure 25. Monotonic grey-scale density is used, with darker colour denoting larger (positive) values of $P(C_{f\theta}, \theta)$. Comparing $P(C_{f\theta}, \theta)$ for the two cases at $\theta = 60°$, where the peak value of the mean-flow $C_{f\theta}(\theta)$ is observed, it can be seen that the dark region for $\alpha = 0.6$ is more concentrated, which implies weaker shedding compared to $\alpha = 0.48$. On the bottom side of the cylinder a similar tendency can be observed at approximately $\theta = 320°$.

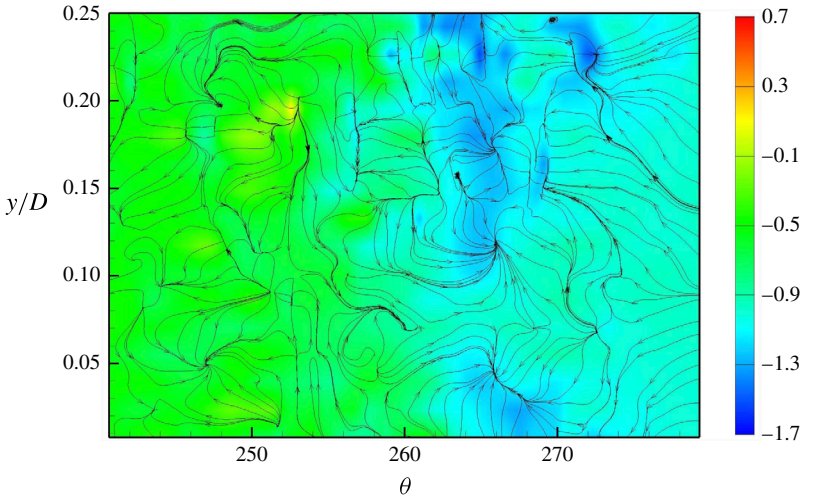

FIGURE 23. (Colour online) Instantaneous pressure field and skin-friction lines for $Re_D = 6 \times 10^4$ and $\alpha = 0.6$.

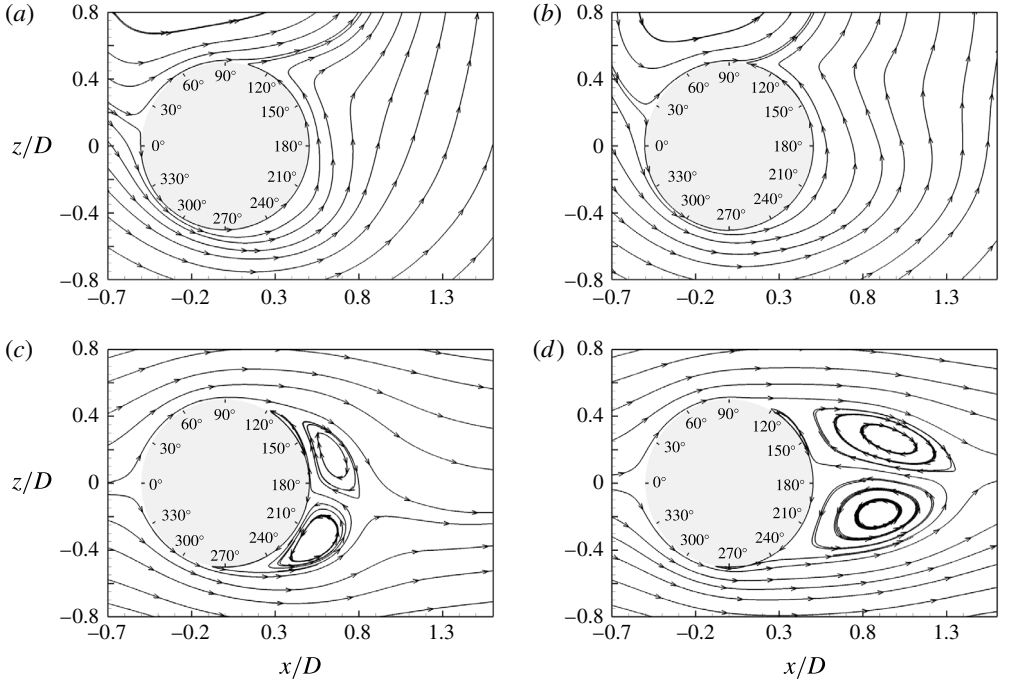

FIGURE 24. Streamlines of the mean velocity for $Re_D = 6 \times 10^4$. (*a*) $\boldsymbol{u}_\alpha(\theta, y, r, t)$ field for $\alpha = 0.48$; (*b*) $\boldsymbol{u}_\alpha(\theta, y, r, t)$ field $\alpha = 0.6$; (*c*) $\boldsymbol{u}(\theta, y, r, t)$ for $\alpha = 0.48$; (*d*) $\boldsymbol{u}(\theta, y, r, t)$ field with $\alpha = 0.6$.

Substantial differences are apparent in the plateau region – the range roughly approximately $110° < \theta < 280°$. For $\alpha = 0.48$, $P(C_{f\theta}, \theta)$ shows broad tails in the $C_{f\theta}$ variable from $\theta = 150°$ to $210°$. This can be attributed to the washing flow, which

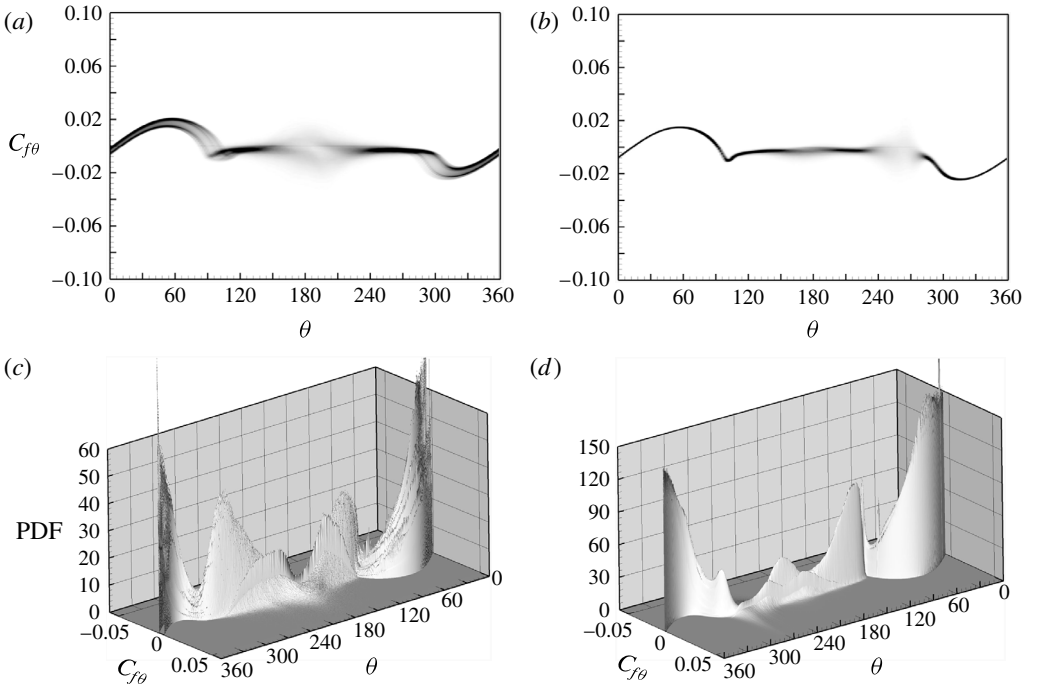

FIGURE 25. PDF of the skin-friction coefficient $C_{f\theta}$ for $Re_D = 6 \times 10^4$. (*a*) $\alpha = 0.48$; (*b*) $\alpha = 0.6$; (*c*) 3D view for $\alpha = 0.48$; (*d*) 3D view for $\alpha = 0.6$.

changes direction gradually and slowly between up-wash and down-wash. For $\alpha = 0.6$, a widely scattered region is found in the range $240° < \theta < 280°$, which covers the bottom of the cylinder. Here $P(C_{f\theta}, \theta)$ is broad in the $C_{f\theta}$ variable, with little dark concentration. From the previous description of the skin-friction lines, we conclude that this region is not related to the presence of washing flow. Instead, it is the result of the aggregation of small-scale separation/reattachment cells, which wrap up the critical points, resulting in chaotic local flow. For the purpose of clarity, 3D views of the two PDFs are shown in figure 25(*c*,*d*), respectively.

5.2. *The γ parameter*

We define the parameter $\gamma(\theta)$ as

$$\gamma(\theta) = \int_0^\infty P(C_{f\theta}, \theta)\, \mathrm{d}C_{f\theta}. \tag{5.2}$$

At fixed θ, $0 \leqslant \gamma(\theta) \leqslant 1$ is a measure of that total fraction of the $C_{f\theta}$ time–spanwise ensemble that are positive, i.e. $C_{f\theta} > 0$. This will now be shown to be a useful statistical metric for locally separated flow.

The streamlines plots of $\boldsymbol{u}_\alpha(r, \theta, y, t)$ clearly show one attachment and one primary-separation line, which broadly divides the flow into two parts. In figure 26, these are denoted regions I and II, respectively. In the sketch, the near-wall flow in region I attaches and flows in a clockwise direction, finally separating at the denoted separation point. Hence at a given θ in region I, if the flow is always attached, then $\gamma = 1$.

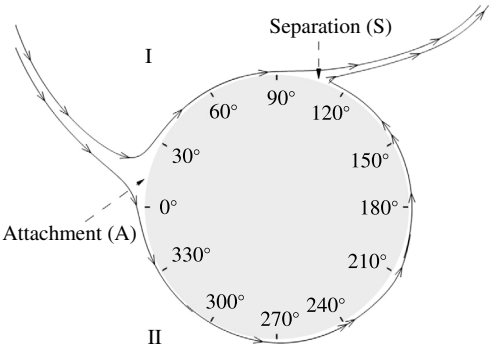

FIGURE 26. Sketch of the configuration of two flow regions: region I and region II. Attachment point (A) and separation point (S) are denoted.

Region	Range on surface	Attached flow	Transitory separation
I	A $\xrightarrow{clockwise}$ S	$C_{f\theta} > 0,\ \gamma = 1$	$\gamma = 0.5$
II	A $\xrightarrow{anticlockwise}$ S	$C_{f\theta} < 0,\ \gamma = 0$	$\gamma = 0.5$

TABLE 5. Flow features of the two regions.

Periods of statistical reversed flow at fixed θ will appear as excursions with $\gamma(\theta)<1$. In contrast, in region II, statistically persistent attached flow at fixed θ will have $\gamma(\theta) = 0$, while reversed or backflow, that is clockwise flow, will show $\gamma(\theta) > 0$. The value $\gamma = 0.5$ is a nominal threshold (Simpson 1989): in region II, $\gamma = 0.5$ corresponds to instantaneous back flow 50 % of the time. Simpson (1989) defines this as transitory separation. A schematic of the flow features in regions I and II is shown in table 5.

In figure 27, we show $\gamma(\theta)$ for all cases at $Re_D = 6 \times 10^4$. Figure 27(*a*) shows $\gamma(\theta)$ with $\alpha = 0$, 0.2 and 0.48. For $\alpha = 0$, the distribution is essentially symmetric about $\theta = 180°$. For this case, $\gamma \approx 0.5$ on the leeward side of the cylinder, indicating transitory separation. Fluctuations about $\gamma \approx 0.5$ occur because primary separation is strongly unsteady during the shedding process. As α increases, the flow is no longer symmetric. On the bottom side of the cylinder the flow tends to be attached. For $\alpha = 0.48$, the flow in region II is generally attached, with a peak region at around $\theta = 180°$, which is clearly associated with up-wash and down-wash flow.

In figure 27(*b*), four cases with $\alpha = 0.48$, 0.52, 0.56 and 0.6 show a different tendency. With increasing α, the peak at around $\theta = 180°$ weakens, while another peak emerges at approximately $\theta = 270°$. For $\alpha = 0.6$, that part of region II where $\gamma \sim 0$ is focused for the most part in the zone $250° < \theta < 280°$, with a relatively sharp peak where γ is close to 0.5. This corresponds to the previously discussed aggregation zone of small-scale separation/reattachment cells, and indicates small-scale but localized transitory separation. With further increase of α the $\gamma(\theta)$ profile does not show new features. The local peak value in region II gradually falls with increasing α.

It is of interest to consider the $\gamma(\theta)$ plot for the lower Re_D flows. In figure 28 for $Re_D = 5 \times 10^3$, the peak at approximately $\theta = 270°$ found at $Re_D = 6 \times 10^4$ at finite α is not observed. Another interesting difference is the behaviour of $\gamma(\theta)$ near primary separation for $\alpha = 0$. For $Re_D = 6 \times 10^4$, γ only reaches $\gamma = 0.5$, which corresponds

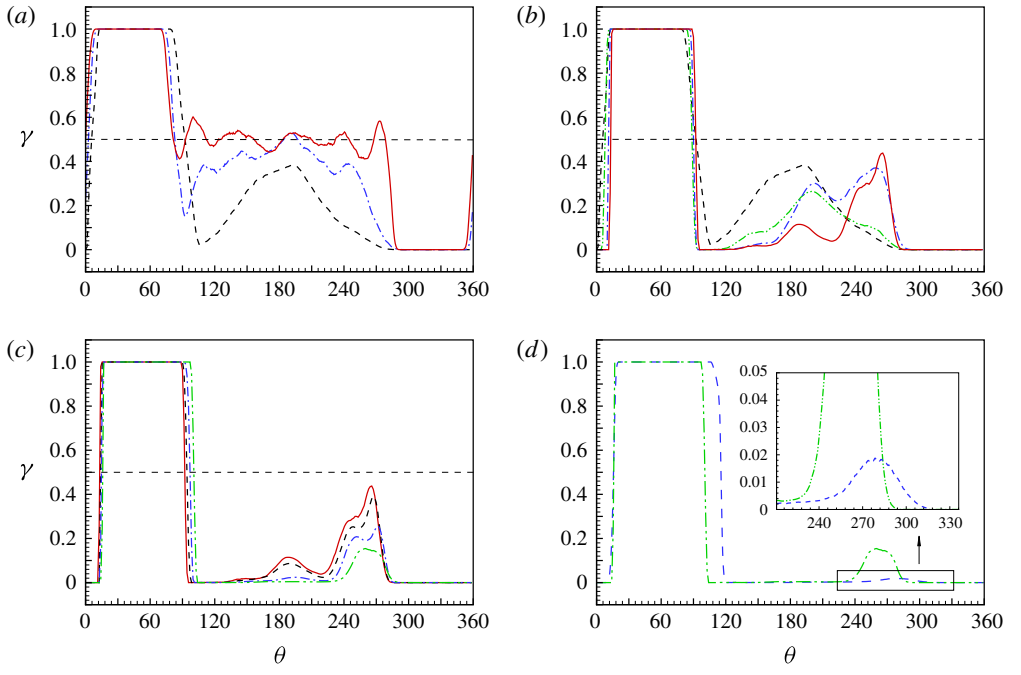

FIGURE 27. (Colour online) γ for $Re_D = 6 \times 10^4$. In (*a*): ——, $\alpha = 0$; — · —, $\alpha = 0.2$, – – – –, $\alpha = 0.48$. In (*b*): – – – –, $\alpha = 0.48$; — · · —, $\alpha = 0.52$, — · —, $\alpha = 0.56$, ——, $\alpha = 0.6$. In (*c*): ——, $\alpha = 0.6$; – – – –, $\alpha = 0.68$; — · —, $\alpha = 0.8$; — · · —, $\alpha = 1.0$. In (*d*): — · · —, $\alpha = 1.0$; – – – –, $\alpha = 2.0$.

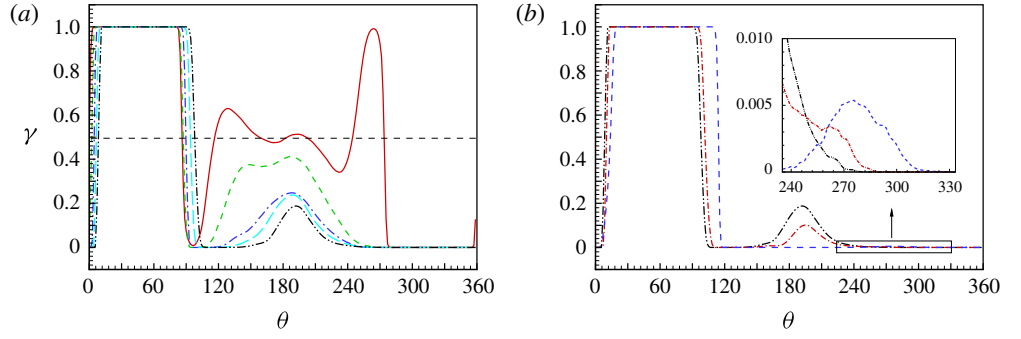

FIGURE 28. (Colour online) γ for $Re_D = 5 \times 10^3$. In (*a*): ——, $\alpha = 0$; – – – –, $\alpha = 0.2$; — · —, $\alpha = 0.4$; ————, $\alpha = 0.6$, — · · —, $\alpha = 0.8$. In (*b*): — · · —, $\alpha = 0.8$; — · —, $\alpha = 1.0$, – – – –, $\alpha = 2.0$.

to 50 % of back flow, implying strong shedding and corresponding movement of the primary-separation line. At $Re_D = 5 \times 10^3$, γ extends to 100 % of back flow, reaches $\gamma = 0$ for the flow on the top side of the cylinder, and $\gamma = 1$ for the flow on the bottom side of the cylinder. This indicates that $Re_D = 5 \times 10^3$ has weak shedding and that the primary-separation lines show little movement.

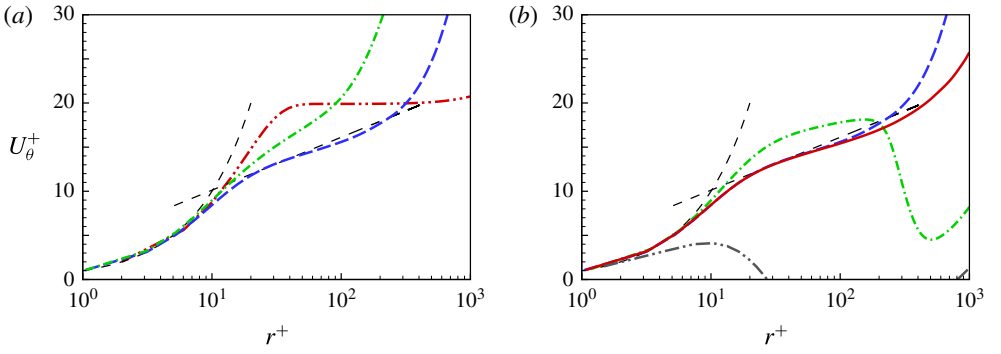

FIGURE 29. (Colour online) Wall-parallel mean-velocity profiles for $Re_D = 6 \times 10^4$ with $\alpha = 1.0$. (*a*) — · · —, 315°; — · —, 247.5°; – – – –, 225°. (*b*) – – – –, 225°; ——, 202.5; — · —, 135°; — · · —, 112.5°. Two dashed reference lines: linear relationship ($U_\theta^+ = r^+$) and log relationship ($U_\theta^+ = \ln(r^+)/k + B$) with $k = 0.378$ and $B = 4.08$.

6. Discussion

6.1. *Wall-parallel velocity profiles: laminar or turbulent?*

For flow over a non-rotating cylinder, near-wall laminar–turbulence transition first occurs on one side of the body within the upper portion of a 'prior' separation bubble for $Re_D > 3.5 \times 10^5$. In the sense of increasing Re_D, this just follows the drag crisis, continuing to $Re_D \approx 10^6$ before the beginning of the trans-critical flow regime (Lehmkuhl *et al.* 2014; Cheng *et al.* 2017). For higher Re_D, the transition zone migrates to the cylinder surface as the prior separation bubble disappears (Roshko 1961). For the flow over a rotating cylinder, turbulence transition is difficult to characterize within the (Re_D–α) plane. The experimental data of Aldoss & Abou-Arab (1990) shows boundary-layer transition at $\alpha = 1.29$ for $Re_D = 4.42 \times 10^4$ while Peller (1986) observes turbulence transition at $\alpha = 1.0$ for $Re_D = 4.8 \times 10^4$. It is therefore of interest to investigate turbulence transition in the present LES in order to clarify its role in the lift crisis.

6.1.1. *Turbulent boundary profiles at* $Re_D = 6 \times 10^4$

We begin with $Re_D = 6 \times 10^4$ with $\alpha = 1.0$ which, according to the reference experiments, might be expected to show turbulence transition on the cylinder surface. Figure 29 shows the wall-parallel, mean-velocity boundary-layer profiles on the bottom side of the cylinder where turbulent transition is expected to first occur. In this plot $U_\theta^+ \equiv U_{\alpha,\theta}/u_\tau$, with $U_{\alpha,\theta}(\theta, r)$ the spanwise–time average of $u_{\alpha,\theta}(\theta, y, r, t)$ (see (4.1)) and $r^+ \equiv (r - D/2)u_\tau/\nu$. Six θ locations are chosen along the direction of flow: $\theta = 315°$, $247.5°$, $225°$, $202.5°$, $135°$, $112.5°$. Two reference lines are also plotted in figure 29: one is a linear relationship while the other is a log relationship $U_\theta^+ = \ln(r^+)/k + B$ with $k = 0.378$ and $B = 4.08$. Up to $\theta = 247.5°$, the velocity profile is still laminar, but at $\theta = 225°$, a clear log-layer can be seen. This log-layer persists up to $\theta = 202.5°$. Further downstream the velocity profile becomes gradually lifted owing to an adverse pressure gradient, tending to show separation behaviour at $\theta = 112.5°$.

Velocity profiles for $\alpha = 0.48$ and $\alpha = 0.6$ at $Re_D = 6 \times 10^4$, are shown in figures 30 and 31, respectively, for six θ locations. For both flows the evolution of the velocity profiles in the near-wall flow direction is initially somewhat similar to the $\alpha = 1$

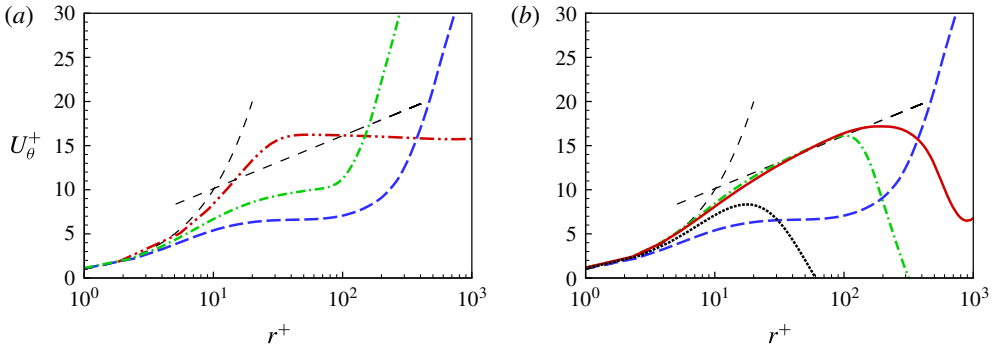

FIGURE 30. (Colour online) Wall-parallel mean-velocity profiles for $Re_D = 6 \times 10^4$ with $\alpha = 0.48$. (*a*) — · · —, 315°; — · —, 247.5°; – – – –, 225°. (*b*) – – – –, 225° ——, 160°; — · —, 135°; · · · · · ·, 112.5°. Two dashed reference lines: linear relationship ($U_\theta^+ = r^+$) and log relationship ($U_\theta^+ = \ln(r^+)/k + B$) with $k = 0.378$ and $B = 4.08$.

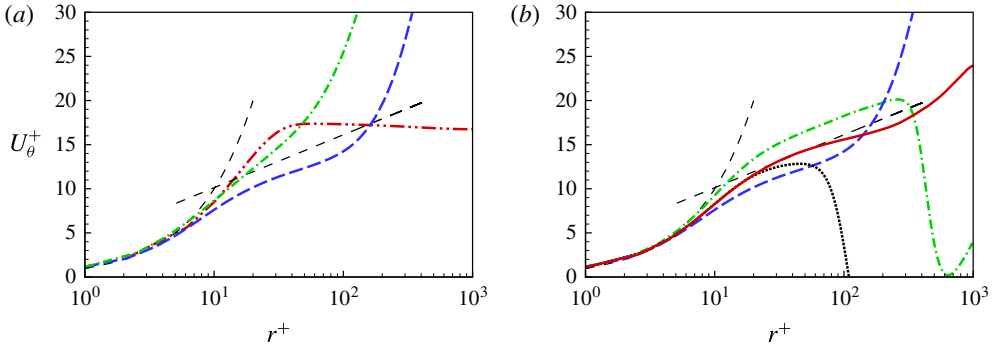

FIGURE 31. (Colour online) Wall-parallel mean-velocity profiles for $Re_D = 6 \times 10^4$ with $\alpha = 0.6$. (*a*) — · · —, 315°, — · —, 247.5°; – – – –, 225°. (*b*) – – – –, 225° ——, 160°; — · —, 135°; · · · · · ·, 112.5°. Two dashed reference lines: linear relationship ($U_\theta^+ = r^+$) and log relationship ($U_\theta^+ = \ln(r^+)/k + B$) with $k = 0.378$ and $B = 4.08$.

flow. Both cases show weak evidence of a log-layer present at 160°, but this is not persistent as for the case $\alpha = 1$. We can conclude that a fully developed turbulent boundary layer is not found for either $\alpha = 0.48$ and $\alpha = 0.6$. In particular, no significant differences in near-wall turbulence characteristics are observed for these two flows.

6.2. *The lift crisis*

Although no quantification exists of critical-point area density in the recirculation region for flow over a stationary cylinder, an intuitively reasonable hypothesis is that the mean distance between critical points, if statistically measurable, should decrease with increasing Re_D. For high-Re_D flow over the stationary cylinder, the surface skin-friction images of Cheng *et al.* (2017) at $Re_D = 10^4$, 10^5 show some indication of an aggregation small-scale separation/reattachment cells, and hence critical points with increasing Re_D, within two zones, one on each side of the cylinder. Between these zones, their figure 26 shows a strong washing flow which is interpreted as

the agent of a dip in the mean-flow pressure distribution at around $\theta = 180°$. Cheng *et al.* (2017) suggest that the critical-point aggregation zones form the fluctuating, area-distributed separation region of an intermediate-scale, mean-flow structure called a secondary-separation bubble, one of which exists on each side of the cylinder at subcritical Re_D. As Re_D increases this secondary-separation bubble together with its reattachment, surface-streamline bundles moves upstream, dynamically interacting with the primary-separation shear layer. Cheng *et al.* (2017) argue that this interaction becomes sufficiently strong to produce an almost discontinuous (in Re_D) transition of the global flow structure characterized by a strong rearward shift in the primary-separation line. This is the drag crisis. It is accompanied by vanishing of the secondary-separation bubble and the appearance of a prior bubble upstream of primary-flow separation.

For the rotating-cylinder flow, for example at $\alpha = 0.6$, a phenomenon associated with the small-scale separation/reattachment cells can also be observed, but with different effects. When the aggregation of small-scale separation/reattachment cells forms near the bottom side of the cylinder in $240° < \theta < 280°$, the attached flow, after dynamical interaction with these separation/reattachment cells, behaves like an adverse pressure gradient flow and forms a low-pressure region. In the rotating-cylinder flow, since there is no primary separation for the flow on the bottom side of the cylinder, this low-pressure region then leads to a suddenly reduced C_L, which is the lift crisis. The crisis is essentially conditioned by the rapid aggregation of wide-area patches of critical points into the relatively narrow band over a quite small range of Re_D.

We have argued that, at $Re_D = 6 \times 10^4$, the lift crisis itself is a result of flow reorganization on the under and leeward parts of the cylinder surface where an aggregation region of small-scale separation/reattachment cells forms in the range $\alpha = 0.48$–0.6. The aggregation zone forms an ordered dividing line separating upstream, almost two-dimensional oncoming flow, from downstream small-scale reversal flows. For even higher Re_D, especially at those values where boundary-layer turbulent transition already exists with $\alpha = 0$, the flow could be more complex. For Re_D around the drag crisis range in the static cylinder case, the cylinder rotation at even small α results in the coalescence of the prior separation bubble and the primary separation, which is directly followed by the flow reorganization phenomenon discussed previously. For even higher Re_D in the supercritical regime, turbulence transition still takes place on the prior separation bubble and, at some finite α, is absorbed by the primary separation.

7. Conclusion

The present study uses wall-resolved large-eddy simulation (LES) in order to provide insight into our understanding of the lift crisis in the flow over a cylinder rotating with constant angular velocity. Here the stretched-spiral vortex SGS model is embedded in a fourth-order curvilinear coordinate code. Cases implemented include an LES set at a lower Re_D at 5×10^3, used both for code verification and also to demonstrate flow behaviour in the absence of a lift crisis, while the LES set at the higher $Re_D = 6 \times 10^4$, $0 \leqslant \alpha \leqslant 2$ provides the basis for the present study. Profiles of both the pressure coefficient C_p and the skin-friction coefficient $C_{f\theta}$ clearly illustrate the presence of a lift crisis from $\alpha = 0.48$ to $\alpha = 0.6$, where α is the non-dimensional rotation speed. This range agrees well with experimental data.

Detailed flow studies are presented for $Re_D = 6 \times 10^4$ with $\alpha = 0.48$ and $\alpha = 0.6$. Instantaneous surface skin-friction portraits indicate that the movement of near-wall,

small-scale reversal flows with increasing α through the lift crisis is a critical flow phenomenon. At $\alpha = 0.48$, the area distribution of small-scale separation/reattachment cells on the cylinder under surface is divided into two loosely scattered groups separated by regions of attached, sloshing flow, presently termed 'washing flow'. The overall under-surface flow is chaotic, with fluctuating, local separation, and small-scale vortex shedding. At $\alpha = 0.6$, a flow reorganization has occurred where the small-scale separation/reattachment cells become aggregated within a region of around $240^\circ < \theta < 280^\circ$, with θ measured in the direction of cylinder rotation from the windward geometrical centreline of the cylinder surface. It is apparent from the skin-friction portraits that this zone is coherent in the spanwise direction, consisting of broadly unidirectional, mainly attached flow, as opposed to washing flow.

This flow scenario is supported by streamlines of the instantaneous, but spanwise-averaged flow field, the latter constructed by subtraction of the solid-body rotation field so that surface skin-friction lines are the wall limit of instantaneous streamlines. Streamlines of the spanwise-averaged velocity field at $\alpha = 0.48$ clearly show the pinch-off of vortices, including a wall-attached separation bubble, which rotates in an anticlockwise direction and is a generator of the wash flow, and an off-wall clockwise vortex. In contrast, for $\alpha = 0.6$, no obvious vortex is generated, which is consistent with the largely attached surface flow and disappearance of the wash flow. This suggests the hypothesis that the aggregation of the small-scale reversal flows, identified on the plot of skin-friction lines as small-scale separation/reattachment cells, is the dominant signature of flow reorganization associated with the onset of the lift crisis.

We further construct a joint probability distribution of $C_{f\theta}$, θ on the cylinder surface from which we define a parameter γ which can be interpreted as a statistical measure of the extent of surface separation/reattachment. The azimuthal distribution of γ clearly shows a region of incipient transitory separation around the bottom (retreating) of the cylinder for cases after the lift crisis, while this phenomenon is not observed for cases before the lift crisis.

In order to explore the issue of boundary-layer laminar–turbulent transition, we have studied the wall-parallel velocity profiles for three flow cases at $Re_D = 6 \times 10^4$. While profiles with $\alpha = 1$ clearly show log-law behaviour characteristic of a turbulent boundary layer, for $\alpha = 0.48$ and $\alpha = 0.6$, log-law type velocity profiles cannot be clearly found. This is taken to indicate that boundary-layer turbulent transition does not play a role in the lift crisis, at least for $Re_D = 6 \times 10^4$.

In summary, visualization of the $\boldsymbol{C_f}$ portraits through a lift cycle together with instantaneous but spanwise-averaged streamline plots of the modified velocity field $\boldsymbol{u}_\alpha(r, \theta, y, t)$ suggests that, at $Re_D = 6 \times 10^4$, the flow on the leeward-bottom surface of the cylinder undergoes a dramatic reorganization. This consists of a transition of patches of scattered, small-scale separation/reattachment cells at $\alpha = 0.48$, separated by regions of wash-type flow and accompanied by separation events sufficiently strong to form both wall-attached and fully separated vortices, to a more ordered state at $\alpha = 0.6$. Here the small-scale separation/reattachment events aggregate into a relatively narrow zone producing both small-scale incoherent separation accompanied by a deep pressure minimum. Hence the lift crisis. The detailed dynamical mechanism of this transition is probably conditioned by the presence of enhanced rotation on the near-wall boundary-layer dynamics.

Acknowledgements

This work was partially supported by the KAUST baseline research funds of R.S. The Cray XC40, Shaheen, at KAUST was utilized for all the reported LES.

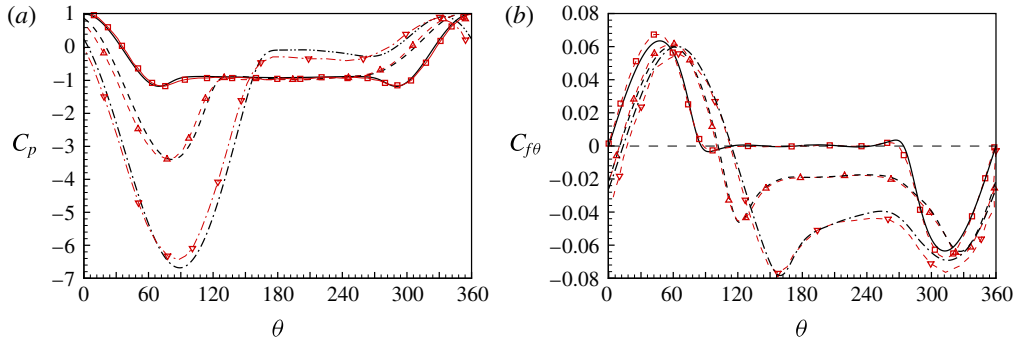

FIGURE 32. (Colour online) Numerical verification at $Re_D = 5 \times 10^3$. (*a*) Pressure coefficient C_p; (*b*) skin-friction coefficient $C_{f\theta}$. Symbols for DNS by Aljure *et al.* (2015): □, $\alpha = 0$; △, $\alpha = 1.0$; ▽, $\alpha = 2.0$. Lines for present LES: ——, $\alpha = 0$; – – – –, $\alpha = 1.0$; — · —, $\alpha = 2.0$.

	C_L		C_D		C_{Lrms}		C_{Drms}
α	DNS	LES	DNS	LES	DNS	LES	LES
0	0.00	0.00	1.05	1.04	0.19	0.23	0.062
1.0	1.40	1.46	0.90	0.91	0.40	0.42	0.10
2.0	4.47	4.64	0.36	0.33	0.08	0.11	0.041

TABLE 6. Comparison of DNS data (Aljure *et al.* 2015) and LES results: lift coefficient C_L, drag coefficient C_D, lift coefficient fluctuation C_{Lrms} and drag coefficient fluctuation C_{Drms}.

Appendix A. Numerical verification

For verification purposes, we consider the reference DNS of Aljure *et al.* (2015) at $Re_D = 5 \times 10^3$, which utilized an unstructured mesh consisting of approximately 40×10^6 cells with 320 cells in the spanwise direction. For the present LES, the total mesh count is approximately 4×10^6 with 64 spanwise cells. We first compare, in figure 32, the present LES profiles for both C_p and $C_{f\theta}$ with the reference DNS results at $Re_D = 5 \times 10^3$, $\alpha = 0$, 1.0 and 2.0. This is considered satisfactory. In table 6, we list the lift and drag coefficients and also the lift coefficient fluctuations for both DNS and LES. The drag coefficient fluctuation C_{Drms} for LES is also shown.

A reasonable verification metric for wall-bounded LES is the wall-normal scale of the near-wall mesh in inner viscous units, defined as $\Delta r^+ = u_\tau \Delta r/\nu$. Figure 33(*a*,*b*) show $\Delta r^+(\theta)$ at $Re_D = 5 \times 10^3$ and $Re_D = 6 \times 10^4$, respectively, for $\alpha = 0$, 1.0 and 2.0. For all cases the maximum Δr^+ are $O(1)$ or smaller. For $Re_D = 6 \times 10^4$ with $\alpha = 1$, $\Delta r^+ \approx 0.5$ on the back side of the cylinder, which corresponds to the observed turbulent boundary-layer region.

For the spanwise domain size, a common test is *a posteriori* spanwise two-point correlation analysis. This has been documented in many wall-bounded flows, such as airfoil (Zhang & Samtaney 2016) and cylinder flows at high Re_D (Lehmkuhl *et al.* 2014). Here we compute the two-point correlation for the spanwise velocity

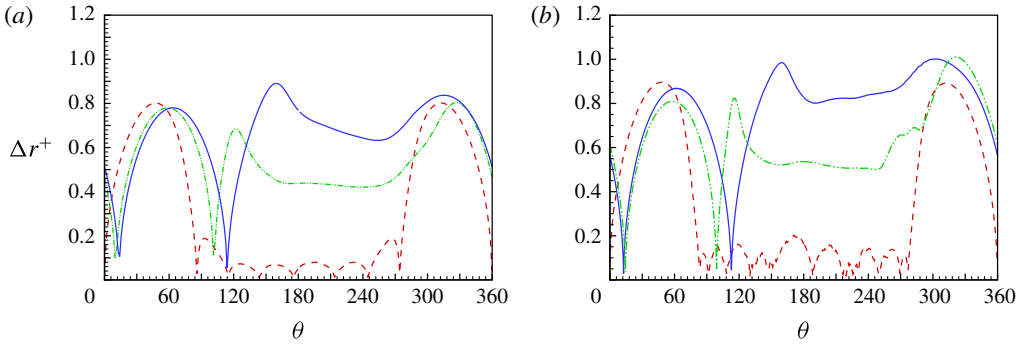

FIGURE 33. (Colour online) Wall-adjacent cell size in wall units: Δr^+. (*a*) $Re_D = 5 \times 10^3$; (*b*) $Re_D = 6 \times 10^4$. – – – –, $\alpha = 0$; — · · —, $\alpha = 1.0$; ——, $\alpha = 2.0$.

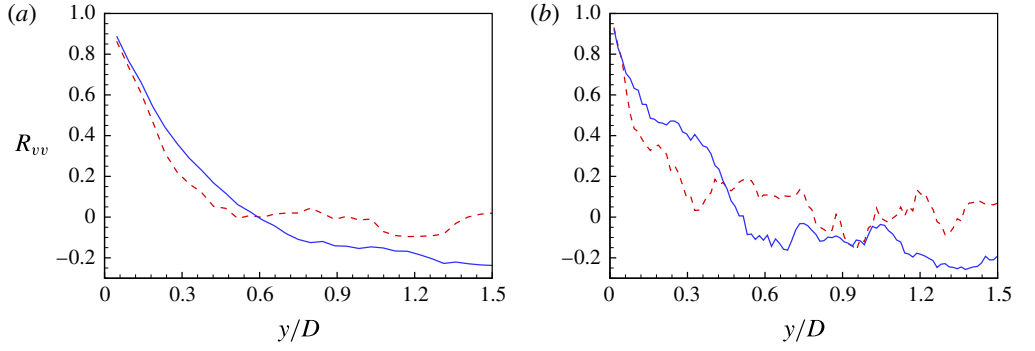

FIGURE 34. (Colour online) Spanwise two-point correlation of spanwise velocity: R_{vv}. (*a*) $Re_D = 5 \times 10^3$. ——, $\alpha = 0$; – – – –, $\alpha = 1$. (*b*) $Re_D = 6 \times 10^4$. ——, $\alpha = 0.48$; – – – –, $\alpha = 0.6$.

component v, defined as

$$R_{vv}(x, y, z) = \frac{\overline{v'(x, 0, z, t)v'(x, y, z, t)}}{\overline{v'(x, 0, z, t)^2}}, \tag{A 1}$$

where the overline denotes a time average. In figure 34, we plot R_{vv} for several cases at $(x, z) = (2D, 0)$, including $\alpha = 0$, 1.0 at $Re_D = 5 \times 10^3$ in figure 34(*a*) and $\alpha = 0.48$ and 0.6 at $Re_D = 6 \times 10^4$ in figure 34(*b*).

Since the main theme of present LES is investigation of the lift crisis phenomenon, mesh-convergence verification is mainly carried out for two cases, $\alpha = 0.48$ and $\alpha = 0.6$. In figures 35 and 36, we compare both C_p and $C_{f\theta}$ for LES using both a coarser mesh with $(N_\theta, N_y, N_r) = (2048, 192, 256)$ and a finer mesh with $(N_\theta, N_y, N_r) = (4096, 384, 512)$. For the two α cases, mesh refinement does not show substantial differences, indicating that our coarser-mesh results are converged.

Appendix B. Subgrid scale model

For wall-resolved LES we utilize the stretched-vortex (SV) SGS model (Misra & Pullin 1997; Voelkl *et al.* 2000; Chung & Pullin 2009), where the subgrid flow is

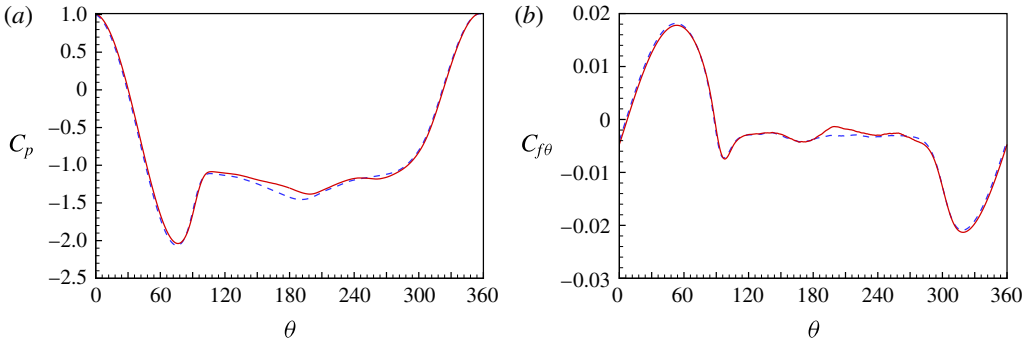

FIGURE 35. (Colour online) Mesh verification case of $\alpha = 0.48$ at $Re_D = 6 \times 10^4$. (*a*) C_p; (*b*) $C_{f\theta}$. – – – –, coarse mesh; ——, fine mesh.

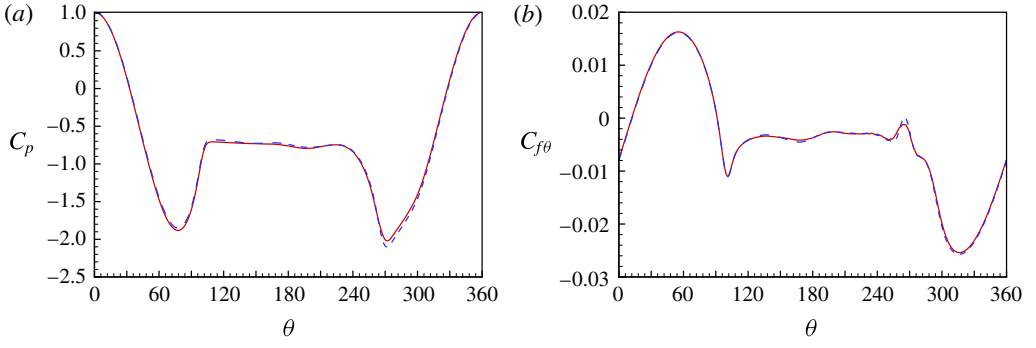

FIGURE 36. (Colour online) Mesh verification case of $\alpha = 0.6$ at $Re_D = 6 \times 10^4$. (*a*) C_p; (*b*) $C_{f\theta}$. – – – –, coarse mesh; ——, fine mesh.

represented by tube/sheet-like structures that are modelled as spiral vortices (Lundgren 1982) stretched by the eddies comprising the local resolved-scale flow. Specifically, in a numerical cell there exists an SGS vortex with direction vector $\boldsymbol{e}^v$, resulting in the subgrid stress

$$T_{ij} = (\delta_{ij} - \boldsymbol{e}_i^v \boldsymbol{e}_j^v)K, \tag{B 1}$$

where K is the subgrid kinetic energy. This is computed from an integral of the SGS energy spectrum as

$$K = \int_{k_c}^{\infty} E(k)\,\mathrm{d}k = \frac{\mathcal{K}_0'}{2}\Gamma\left[-1/3, \frac{2\nu k_c^2}{3|\tilde{a}|}\right]. \tag{B 2}$$

Here $k_c = \pi/\Delta_c$ is the cutoff wavenumber, $\tilde{a} = \boldsymbol{e}_i^v \boldsymbol{e}_j^v \widetilde{\mathcal{S}}_{ij}$ is the stretching along the subgrid vortex with $\widetilde{\mathcal{S}}_{ij}$ the local resolved-scale, rate-of-strain tensor. In the present implementation, the $\boldsymbol{e}_j^v$ are aligned with the principal extensional eigenvector of $\widetilde{\mathcal{S}}_{ij}$. The grouped constant $\mathcal{K}_0'$ is calculated from the resolved-scale velocity using a matching procedure as $\mathcal{K}_0' = \langle F_2 \rangle / \langle Q(\kappa_c, d) \rangle$, where $\langle \cdots \rangle$ denotes an averaging strategy, computed as the arithmetic mean of 26 neighbouring points and $\kappa_c = k_c(2\nu/3|\tilde{a}|)^{1/2}$ (Chung & Pullin 2009). The quantity F_2 is a second-order velocity difference of the resolved-scale velocity field between two points, $Q(\kappa_c, d)$ is calculated using an

asymptotic approximation to an integral with $d = r/\Delta_c$, where r is the distance of the cell centre to the neighbouring point. The model implementation is dynamic with no adjustable parameters. For details, see Misra & Pullin (1997), Voelkl *et al.* (2000), Chung & Pullin (2009).

REFERENCES

ACHENBACH, E. 1968 Distribution of local pressure and skin friction around a circular cylinder in cross-flow up to $Re = 5 \times 10^6$. *J. Fluid Mech.* **34**, 625–639.

ALDOSS, T. K. & ABOU-ARAB, T. W. 1990 Experimental study of the flow around a rotating cylinder in crossflow. *Exp. Therm. Fluid Sci.* **3** (3), 316–322.

ALJURE, D. E., RODRÍGUEZ, I., LEHMKUHL, O., PÉREZ-SEGARRA, C. D. & OLIVA, A. 2015 Influence of rotation on the flow over a cylinder at $Re = 5000$. *Intl J. Heat Fluid Flow* **55**, 76–90.

CARSTENSEN, S., MANDVIWALLA, X., VITA, L. & PAULSEN, U. S. 2014 Lift of a rotating circular cylinder in unsteady flows. *J. Ocean Wind Energy* **1**, 41–49.

CHENG, W., PULLIN, D. I. & SAMTANEY, R. 2018 Large-eddy simulation of flow over a grooved cylinder up to transcritical Reynolds numbers. *J. Fluid Mech.* **835**, 327–362.

CHENG, W., PULLIN, D. I., SAMTANEY, R., ZHANG, W. & GAO, W. 2017 Large-eddy simulation of flow over a cylinder with Re_D from 3.9×10^3 to 8.5×10^5: a skin-friction perspective. *J. Fluid Mech.* **820**, 121–158.

CHONG, M. S., SORIA, J., PERRY, A. E., CHACIN, J., CANTWELL, B. J. & NA, Y. 1998 Turbulence structures of wall-bounded shear flows found using DNS data. *J. Fluid Mech.* **357**, 225–247.

CHUNG, D. & PULLIN, D. I. 2009 Large-eddy simulation and wall modelling of turbulent channel flow. *J. Fluid Mech.* **631**, 281–309.

DRYDEN, H. L., MURNAGHAN, F. D. & BATEMAN, H. 1932 Report of the Committee on Hydrodynamics. *Tech. Rep.* 84. National Research Council.

FLETCHER, C. A. J. 1972 Negative Magnus forces in the critical Reynolds number regime. *J. Aircraft* **9** (12), 826–834.

KIM, J., CHOI, H., PARK, H. & YOO, J. Y. 2014 Inverse Magnus effect on a rotating sphere: when and why. *J. Fluid Mech.* **754**, R2.

LEHMKUHL, O., RODRÍGUEZ, I., BORRELL, R., CHIVA, J. & OLIVA, A. 2014 Unsteady forces on a circular cylinder at critical Reynolds numbers. *Phys. Fluids* **26** (12), 125110.

LUNDGREN, T. S. 1982 Strained spiral vortex model for turbulent fine structure. *Phys. Fluids* **25** (12), 2193–2203.

MISRA, A. & PULLIN, D. I. 1997 A vortex-based subgrid stress model for large-eddy simulation. *Phys. Fluids* **9** (8), 2443–2454.

MITTAL, S. & KUMAR, B. 2003 Flow past a rotating cylinder. *J. Fluid Mech.* **476**, 303–334.

MORINISHI, Y., LUND, T. S., VASILYEV, O. V. & MOIN, P. 1998 Fully conservative higher order finite difference schemes for incompressible flow. *J. Comput. Phys.* **143** (1), 90–124.

PELLER, H. 1986 Thermofluiddynamic experiments with a heated and rotating circular cylinder in crossflow. II – Boundary layer profiles and location of separation points. *Exp. Fluids* **4**, 223–231.

REID, E. G. 1924 Tests of rotating cylinders. *Tech. Rep.* 209. National Advisory Committee for Aeronautics.

ROSHKO, A. 1961 Experiments on the flow past a circular cylinder at very high Reynolds number. *J. Fluid Mech.* **10** (03), 345–356.

SCHEWE, G. 1983 On the force fluctuations acting on a circular cylinder in crossflow from subcritical up to transcritical Reynolds numbers. *J. Fluid Mech.* **133**, 265–285.

SIMPSON, R. L. 1989 Turbulent boundary-layer separation. *Annu. Rev. Fluid Mech.* **21**, 205–234.

SON, J. S. & HANRATTY, T. J. 1969 Velocity gradients at the wall for flow around a cylinder at Reynolds numbers from 5×10^3 to 10^5. *J. Fluid Mech.* **35** (2), 353–368.

SWANSON, W. M. 1961 The Magnus effect: A summary of investigations to date. *Trans. ASME: J. Basic Engng* **83** (3), 461–470.

TAKAYAMA, S. & AOKI, K. 2005 Flow characteristics around a rotating grooved circular cylinder with grooved of different depths. *J. Vis.* **8** (4), 295–303.

THOM, A. 1931 Experiments on the flow past a rotating cylinder. *Tech. Rep.* 1410. Reports and Memoranda.

THOM, A. 1934 Effect of discs on the air forces on a rotating cylinder. *Tech. Rep.* 1623. Reports and Memoranda.

VOELKL, T., PULLIN, D. I. & CHAN, D. C. 2000 A physical-space version of the stretched-vortex subgrid-stress model for large-eddy simulation. *Phys. Fluids* **12**, 1810–1825.

ZHANG, W., CHENG, W., GAO, W., QAMAR, A. & SAMTANEY, R. 2015 Geometrical effects on the airfoil flow separation and transition. *Comput. Fluids* **116**, 60–73.

ZHANG, W. & SAMTANEY, R. 2016 Low-*Re* flow past an isolated cylinder with rounded corners. *Comput. Fluids* **136**, 384–401.